Summer 2015

Differential Incision and Uplift of the Yakima River Terraces

Adrian M. Bender
Western Washington University, adrianmbender@gmail.com

Differential Incision and Uplift of the Yakima River Terraces

by

Adrian M. Bender

Accepted in Partial Completion

Of the Requirements for the Degree

Master of Science

Kathleen L. Kitto, Dean of the Graduate School

ADVISORY COMMITTEE

Dr. Colin Amos

Dr. Elizabeth Schermer

Dr. Brian L. Sherrod

MASTER'S THESIS

In presenting this thesis in partial fulfillment of the requirements for a master's degree at Western Washington University, I grant to Western Washington University the non-exclusive royalty-free right to archive, reproduce, distribute, and display the thesis in any and all forms, including electronic format, via any digital library mechanisms maintained by WWU.

I represent and warrant this is my original work, and does not infringe or violate any rights of others. I warrant that I have obtained written permissions from the owner of any third party copyrighted material included in these files.

I acknowledge that I retain ownership rights to the copyright of this work, including but not limited to the right to use all or part of this work in future works, such as articles or books.

Library users are granted permission for individual, research and non-commercial reproduction of this work for educational purposes only. Any further digital posting of this document requires specific permission from the author.

Any copying or publication of this thesis for commercial purposes, or for financial gain, is not allowed without my written permission.

Adrian Bender

June 2015

Differential Incision and Uplift of the Yakima River Terraces

A Thesis
Presented to
The Faculty of
Western Washington University

In Partial Fulfillment
Of the Requirements for the Degree
Master of Science

by
Adrian M. Bender
June, 2015

Abstract

The Yakima fold belt comprises fault-related folds deforming Miocene basalts and younger deposits of the Columbia Plateau in central Washington State. Geodesy implies ~2 mm/yr of modern, NNE-directed regional shortening; however the distribution of Quaternary deformation among individual structures remains unclear. South of Ellensburg, Washington, the Yakima River cuts a ~600-m deep canyon across several of the folds, preserving flights of strath terraces that record the progressive incision. Graded alluvial basins at the head and mouth of the canyon imply that terrace incision also records differential rock uplift. We integrate lidar analysis, field observations, and cosmogenic burial dating of eight strath terraces in the canyon to quantify Quaternary incision across two folds, Manastash Ridge and Umtanum Ridge.

Isochron burial ages from in-situ ^{26}Al and ^{10}Be characterize four terrace-forming intervals at ≤0.5 Ma, 0.7 -1.3 Ma, 1.5-1.7 Ma, and 2.8-3.0 Ma. Along with the burial ages, we use lidar-derived strath heights to calculate time-averaged bedrock incision rates of ~10^{-3} mm/yr through synclinal lows, and ~10^{-2} within the Manastash and Umtanum Ridge anticlines (~0.07 mm/yr from 0.2-0.4 Ma and ~0.04 mm/yr from 1.5-1.7 Ma, respectively). Collectively, the results demonstrate Quaternary differential bedrock incision and uplift of the Manastash and Umtanum Ridge anticlines. Incision rates permit horizontal shortening at ~0.08-0.12 mm/yr across master faults (dip 30±10° S) beneath the folds, indicating that other compressional structures in the region likely take up the remaining ~1-2 mm/yr of modern regional geodetic shortening.

Acknowledgements

Table of Contents

List of tables

List of figures

1. Comprehensive introduction

This thesis manuscript, "Differential uplift and incision of the Yakima River terraces", has also been submitted for review and potential publication in *JGR Solid Earth*. The authors of the submitted paper are (in order): Adrian Bender, Colin Amos, Paul Bierman, Dylan Rood, Lydia Staisch, Harvey Kelsey, and Brian Sherrod. Bender, Amos, Rood, Kelsey and Sherrod conducted field reconnaissance. Bender conducted field and lidar-based geologic mapping and surveying. Bender, Amos, and Rood sampled terrace gravels for burial ages. Bender and Bierman prepared samples for accelerator mass spectrometer analysis of ^{26}Al and ^{10}Be. Rood conducted accelerator mass spectrometer analysis of sample ^{26}Al and ^{10}Be. Staisch provided the MATLAB script used for linear regression analysis. Bender analyzed lidar and cosmogenic data, calculated all reported ages, rates, and uncertainties; wrote the manuscript, and prepared all tables and figures. Amos, Bierman, Rood, Staisch, Kelsey and Sherrod reviewed and edited the manuscript and figures.

Our paper presents original data and results from ^{26}Al-^{10}Be geochronology, aerial lidar analysis, and geomorphic mapping to assess Quaternary fluvial bedrock incision and uplift in the Yakima fold belt, a region of the Cascadia backarc that actively accommodates distributed plate boundary strain with modest shortening. We use a suite of fluvial strath terraces along the Yakima River to calculate average rates of differential bedrock uplift and incision over the past ~2.9 m.y. across two anticlines that may link the fold belt to Holocene-active faults in the Cascadia forearc. Our results provide the first quantitative estimates of Quaternary bedrock incision, uplift and shortening in the Yakima fold belt, and show that a substantial portion of regional geodetic shortening remains unaccounted for, with clear implications for Yakima fold belt seismic hazard.

2. Introduction

A comprehensive understanding of upper-plate deformation along active convergent margins requires measurements of geologic deformation spanning 10^0 to 10^6 yr intervals, and over spatial scales sufficient to capture the influence of key tectonic structures. Relatively few such locales offer a complete spatial and temporal record of deformation, however, leaving knowledge gaps that pose critical issues for seismic hazard analyses (e.g., Petersen et al., 2014). The Cascadia convergent margin in the US Pacific Northwest represents a locale where GPS geodesy measures regional strain accumulation far inboard of the subduction zone over several decades (Figure 1 inset), but cannot resolve strain across individual faults and folds whose activity spanning 10^2 to 10^6 yr remains largely unknown (McCaffrey et al., 2013)

Oblique Pacific-North American plate motion along with Basin and Range extension distributed across the Cascadia convergent margin drives clockwise rotation of the western Oregon forearc, which in turn drives shortening on both sides of the Cascade volcanic arc in Washington (Figure 1) (McCaffrey et al., 2013; Wells and McCaffrey, 2013; Wells et al., 1998). East-west and northwest striking-forearc faults between northwestern Oregon and Washington reveal Quaternary to Holocene reverse faulting (Blakely et al., 2002; Johnson et al., 1999; Johnson et al., 1996; Kelsey et al., 2012; Kelsey et al., 2008; Nelson et al., 2003; Sherrod et al., 2013; Sherrod et al., 2008; Sherrod et al., 2004) at rates roughly consistent with geodetically observed shortening (McCaffrey et al., 2013). McCaffrey et al. (2013) also suggest that the faulted anticlines of the Yakima fold belt (Figure 1) accommodate backarc geodetic shortening, although the distribution of shortening among specific structures remains unknown.

Geologic evidence for recent tectonic deformation in the Yakima fold belt is limited. Paleoseismic investigations of tectonic scarps, offset landforms and faulted stratigraphy reveal

2

evidence for late Pleistocene to Holocene deformation on several Yakima fold belt structures (Blakely et al., 2011; Campbell and Bentley, 1981; Ladinsky, 2012; Reidel, 1984; West et al., 1996). Repeated late Pleistocene Lake Missoula floods (Bretz, 1969; Waitt, 1980, 1985), limit the preservation of landforms and deposits recording earlier Quaternary deformation. The resulting lack of geochronologic constraints on Cascade backarc deformation is particularly significant given recent studies identifying subsurface geophysical anomalies that may connect the Yakima fold belt to Holocene-active forearc faults in the Puget Sound region (Blakely et al., 2011, 2014).

The importance of establishing Quaternary geochronologic constraints on the deforming Yakima fold belt structures is two-fold. First, knowing geologic deformation rates will establish the relative contribution of Quaternary folding and faulting to the tectonic development of the Yakima fold belt and the Cascade backarc. For example, some workers postulate structural development of the Yakima folds and faults entirely between ~2.9 and 10.5 Ma (e.g., Reidel, 1984), but the lack of geochronologic constraints on younger deformation leaves this assertion untested. Second, while geodesy demonstrates ~2 mm/yr of shortening across the Yakima fold belt (McCaffrey et al., 2013), it remains uncertain which structures actively accommodate the measured surface deformation. This uncertainty represents a significant gap in the current assessment of Pacific Northwest seismic hazards, especially given the $\geq M_w 7$ seismic potential of Yakima fold-belt faults proximal to the Hanford nuclear site (Figure 1) (Wells and Coppersmith, 1994; Blakely et al., 2011).

This investigation focuses on the Yakima River Canyon, located south of the Kittitas Valley, Washington (Figure 1). Here, the Yakima River incises a meandering canyon up to ~600 m deep and nearly perpendicular to strike across three of the Yakima folds: Manastash Ridge,

Umtanum Ridge, and Selah Butte, from north to south (Figure 2a). The presence of alluvial

basins up- and downstream of the basalt-floored canyon suggests that canyon incision is a direct

response to folding and uplift of the basaltic block. The canyon contains a suite of predominately

unpaired strath terraces that consist of both local (basaltic) and Cascade Mountains-derived

gravels (mixed rock type) overlying straths cut in Miocene basalts.

We use quartz-bearing clasts in the Yakima terrace gravels to quantify differential

incision across the Manastash and Umtanum Ridge folds by employing ^{26}Al-^{10}Be isochron burial

dating (Balco and Rovey, 2008; Çiner et al., 2014; Erlanger et al., 2012; Darling et al., 2012) to

estimate the age of the terraces. We use lidar and field observations to constrain terrace strath

height above the modern Yakima River. Comparison of incision rates from dated terrace deposits

both within and outside the canyon enables measurement of fluvial downcutting driven by uplift

and deformation of the Yakima folds. We infer rock uplift rates from incision, and relate these

rates to horizontal shortening on underlying reverse-fault-related anticlines (Casale and Pratt;

2015; Ladinsky, 2012; Miller, 2014). Together, our results provide the first quantitative estimate

of late Quaternary deformation rates across these structures and their relative contribution to the

total modern budget of shortening and potential seismic hazard across the Yakima fold belt.

3. Location and geologic framework

The Yakima fold belt is a structural province of the western Columbia Plateau in south-

central Washington and north-central Oregon (Figure 1). The deformation belt comprises 14

anticlines developed in the Miocene flows and intercalated sediments of the Columbia River

Basalt Group (e.g., Reidel, 1984), as well as in overlying Plio-Pleistocene fluvial and lacustrine

units (e.g., Bingham and Grolier, 1966; Waitt, 1979; Campbell and Bentley, 1981). Blind

thrusting appears to control folding on the anticlines (e.g., Yeats, 2012; Casale and Pratt, 2015), which are primarily north-to-northeast directed and trend east-northeast to west-northwest (e.g., Reidel, 1984). Topography mimics Yakima fold belt structure, with folds expressed as relatively high, narrow anticlinal ridges and broad intervening synclinal valleys. Fold wavelengths range from ~5-35 km (Figure 1) (Watters, 1988, 1989). Individual anticlinal ridges commonly exceed 100 km in length (Figure 1), and typically consist of a steep, north-dipping forelimb thrust over an adjacent, gently south-dipping backlimb (e.g., Reidel, 1984).

Based on geophysical evidence, Saltus (1993) and Pratt (2012) suggest that initial development of the Yakima folds and faults may have started prior to the emplacement of the Columbia River Basalts. Since early descriptions and mapping of the Yakima fold belt structures by Russell (1893) and Smith (1903), workers proposed various mechanisms for their origin, including wrinkle ridges analogous to those identified on Mars (Watters, 1988, 1989) and splay faults related to pre-Miocene dextral shear on the Olympic Wallowa Lineament (OWL) (Hooper and Conrey, 1989; Pratt, 2012; Raisz, 1945). The OWL (Raisz, 1945) (Figure 1) represents a swath of aligned topographic features, including several Yakima folds, extending across the Cascade volcanic arc, from the Wallowa Mountains in Oregon to the Olympic Peninsula in Washington. GPS measurements resolve contemporary shortening across the Yakima fold belt and the OWL (McCaffrey et al., 2013), and Wells and McCaffrey (2013) attribute the deformation to distributed Cascade margin strain consistent with regional geology spanning the past 16 m.y.

Yakima fold belt structures record ~25 km of north-south shortening since the youngest deformed member of the Columbia River Basalts erupted at 10.5 Ma (Reidel, 1984). The average shortening rate since 10.5 Ma (~2.4 mm/yr) is similar to the geodetic rate (1.9 ± 0.5 mm/yr NNE)

(McCaffrey et al., 2013), but does not resolve the rate and distribution of geologically recent deformation on individual Yakima fold belt structures. The geodetic shortening, along with contemporary seismicity (Blakely et al., 2012; Gomberg et al., 2012; Wicks et al., 2011) and paleoseismic evidence (Campbell and Bentley, 1981; Reidel, 1984; West et al., 1996; Blakely et al., 2011; Ladinsky, 2012) collectively suggest continuing tectonic development of the Yakima fold belt through the Quaternary.

Despite nearly 50 years of investigation, geochronologic data constraining Quaternary deformation across the Yakima fold belt remain relatively sparse. Tectonically offset geomorphic surfaces documented in the Kittitas Valley (Waitt, 1979), on Toppenish Ridge in the southern Yakima fold belt (Campbell and Bentley, 1981), on the Saddle Mountains (West et al., 1996), and at numerous disparate locations across the Yakima fold belt (Reidel, 1984) provide some evidence for Late Quaternary and Holocene deformation.

In light of potential structural links between the Yakima fold belt and Holocene-active faults in the Puget Sound (Blakely et al., 2011; 2014), renewed efforts to constrain the timing of Quaternary Yakima fold belt deformation have focused on structures within and adjacent to the OWL. Blakely et al. (2011) trenched two scarps on Umtanum Ridge, revealing up to three episodes of bending-moment-faulting above a hypothesized blind thrust. All three ruptures offset a 47 ka tephra, with the youngest inferred event cutting all Quaternary stratigraphy except the uppermost (modern?) soil.

The Yakima River Canyon (Figure 2) provides several opportunities for characterizing Quaternary deformation. The canyon occupies a unique physiographic location south of the furthest Yakima glacial advance (Porter, 1976), and remained isolated from inundation and scour by the Lake Missoula outburst floods (Bretz, 1969; Waitt, 1980, 1985). The Yakima River

traverses graded alluvial basins to the north and south of the bedrock canyon. Given

comparatively modest incision in these bounding basins, cutting of the ~600 m deep canyon

requires a significant component of differential rock uplift. The uniform durability of the

Miocene Columbia River Basalts flooring the canyon suggests that variations in channel

substrate do not substantially affect fluvial downcutting in the canyon (e.g., Duvall et al., 2004).

The unpaired strath terraces and associated gravel deposits flanking Manastash and Umtanum

Ridges should therefore provide a relatively complete record of Quaternary bedrock incision and

uplift across these structures (Figure 2).

4. Methods

4.1 Surficial mapping

We mapped the surficial geology of the Yakima River Canyon using field observations

and analysis of GeoEarthScope airborne lidar data accessed through the Open Topography portal

(www.opentopography.org). We mapped the canyon between the Selah Valley to the south and

Potato Hill in the Kittitas Valley to the north (Figure 2). We adopt bedrock mapping from the

Washington DNR 1:100,000-scale geologic map database (Schuster, 1994; Walsh, 1986). We

group the Grand Ronde and Wanapum flows of the Columbia River Basalts, along with the

comparatively thin (tens of m thick) Vantage sedimentary horizon of the Ellensburg Formation,

as undifferentiated Tertiary bedrock. Using lidar derivatives (e.g., hillshades, slope maps,

contours) we mapped Quaternary landforms and deposits including terraces, landslides, alluvial

fans, loess, and colluvium at a scale of 1:20,000. We mapped remnant strath terraces from field

observations at a scale of 1:5,000 (Figure 2). We also mapped Selah Butte, the southernmost of

the three anticlines incised by the Yakima River Canyon (Figure 2a), but our field investigation

revealed no exposed strath terraces above the modern channel. We speculate that the lack of

exposed strath terraces across Selah Butte reflects the abundance of large landslides into the

canyon across this fold (Figure 2a).

None of the 14 mapped strath terraces include a paired remnant on the opposite side of

the river (see the supplementary materials for a complete description of terrace deposits and

stratigraphy). Accordingly, correlation of terraces downstream relies on overlapping numerical

ages, and extrapolation between dated sites relies on geomorphic relationships determined from

mapping and lidar analysis. We selected eight strath-capping gravel deposits occupying a range

of structural positions and heights above the active channel to sample for ^{26}Al-^{10}Be isochron

burial dating.

4.2 ^{26}Al-^{10}Be isochron burial dating and sampling

We employ the cosmogenic ^{26}Al-^{10}Be isochron burial dating method (Balco and Rovey,

2008; Erlanger et al., 2012) to determine burial ages for strath-capping terrace gravels and

establish bounds on the timing of terrace formation. The ^{26}Al-^{10}Be isochron burial method

provides several key advantages for dating the Yakima River terrace gravels in comparison to

other Quaternary methods. First, the isochron burial method works well for deposits between 0.2

and 4.0 Ma (Balco and Rovey, 2008). Given the 3.64 ± 0.37 (1σ) Ma age of the highest surface

incised by the Yakima River in the northern Kittitas Valley (Waitt, 1979), we expected the

terrace gravels in the canyon downstream to fall within this range. Also, the method does not

require explicit knowledge of post-burial exposure, erosion, and shielding. Furthermore, terrace

gravels contain quartz-bearing clasts that are, exotic to the basalt-floored canyon, and likely

Cascade Mountains-derived. The Cascade Mountain source requires ~100 km of transport by the

Yakima River to place the exotic gravels in the basalt canyon, and therefore permits associating the strath terrace deposits with the main Yakima River channel. Finally, the quartz in the Cascade-derived clasts provides an inventory of in-situ ^{26}Al and ^{10}Be concentrations that record the timing of deposition.

Like most other cosmogenic burial dating techniques (e.g., Granger, 2006), the isochron method leverages the fixed ratio of in-situ ^{26}Al and ^{10}Be production in quartz exposed at the surface, R_{init} (6.75 ^{26}Al:^{10}Be atoms), and the differential rates of isotope decay after surface production stops. The decay constants λ_{26} (9.83 ± 0.25 x 10^{-7} atoms/yr) and λ_{10} (5.10 ± 0.26 x 10^{-7} atoms/yr) define rates of nuclide decay corresponding with half-lives of 0.705 m.y. for ^{26}Al (Nishiizumi, 2004) and 1.36 m.y. for ^{10}Be (Chmeleff et al., 2010; Nishiizumi et al., 2007).

Unlike other cosmogenic burial dating techniques, the isochron burial method does not require information about the depth, exposure duration, or post-burial nuclide production of the samples (Balco and Rovey, 2008). Instead, the isochron method requires sampling clasts with a wide range of isotope concentrations that record varying (but unknown) pre-burial exposure histories, but common post-burial production and decay. Sampling multiple clasts from the same depth horizon in a given deposit generally achieves these requirements, which are important for dating the Yakima River gravels because (1) the deposits tend to be relatively thin (≤5 m) and may therefore be susceptible to post-burial nuclide production, and (2) we lack information about the pre-burial exposure history and thus nuclide inheritance of the samples we collected.

The slope (R_M) of a line fit to measured nuclide concentrations from clasts collected at each deposit plotted as ^{10}Be versus ^{26}Al reflects the deviation from the surface production ratio (R_{init}) (Figure S1a-c). Because this deviation is dependent on isotope half-life and duration of decay, burial age (t_b) is then calculated as:

(1) $t_b = -\ln(R_m/R_{init}) / (\lambda_{26} - \lambda_{10})$

We collected 15 quartz-bearing cobbles, plus several kg of sand and pebbles from within a 20-30 cm-thick horizon at least 2 m below the top of each strath-capping gravel deposit (Table 1). In order to ensure that our ages best represent the timing of terrace formation, we sampled from directly above the strath whenever possible. All samples were prepared at the University of Vermont Cosmogenic Isotope Laboratory facilities following standard lab protocols (e.g., Corbett et al., 2011). Sample $^{26}Al/^{27}Al$ and $^{10}Be/^{9}Be$ ratios were measured on the Scottish Universities Environmental Research Centre accelerator mass spectrometer (AMS) in East Kilbride, Scotland (Xu et al., 2015). The supplemental material provides a detailed description of sample preparation, AMS measurement, and blank correction.

The main sources of analytic uncertainty contributing to ^{26}Al-^{10}Be isochron burial ages are errors on the nuclide decay constants (~3%), and uncertainties related to AMS measurements (Balco and Rovey, 2008). Decay constant uncertainties contribute uniformly to each burial age, but measurement uncertainties vary. Hence, ^{26}Al-^{10}Be isochron analyses require a linear regression technique that weighs the measurement uncertainties related to each plotted concentration. Previous ^{26}Al-^{10}Be isochron burial age studies (e.g., Balco and Rovey, 2008; Çiner et al., 2015; Darling et al., 2012; Erlanger et al., 2012) use the regression method of York (1966) to address this issue, but we employ a Bayesian approach to linear regression, developed by D'Agostini (2003, 2005) and first applied to ^{26}Al-^{10}Be isochron burial dating isochrons by Muzikar (2011).

The Bayesian approach varies from the York method in two ways. First, rather than assuming uncorrelated slope and errors in fitting a single optimum line to data, Bayesian linear regression tests the likelihood of many slope and intercept value combinations fitting data with x and y errors, and resolves correlation between the modeled parameters. Normalized relative probability distributions of modeled slope and intercept estimate confidence around the most likely estimate of each parameter, and may or may not be Gaussian. The normalized relative probability distributions in this study do tend to be Gaussian, so we consider the 68% confidence interval as the 1σ uncertainty. Second, the Bayesian method allows investigators to constrain modeled regression parameter output based on *a priori* geologic information. For example, the age of a gravel deposit cannot be less than zero; therefore, the slope of a line fit to an isochron plot of ^{26}Al and ^{10}Be concentrations cannot be greater than R_{init} (the slope corresponding to the surface production ratio of ^{26}Al/^{10}Be, nominally 6.75). Hence, 6.75 is a suitable upper limit for modeled slope output.

We use a MATLAB script implementing Bayesian linear regression statistics to construct ^{26}Al-^{10}Be burial isochrons. The script runs a Monte Carlo simulation algorithm to fit a chosen number of lines to bivariate data with associated errors within optionally specified windows of slope and intercept, and calculates likelihood of fit for each line. The parameters with the highest calculated likelihood are the most likely estimated values (D'Agostini, 2003). Using this methodology, we test the likelihood of 100,000 lines having slopes between 0 and 6.75 fit to ^{26}Al and ^{10}Be concentration data from each of the eight sampled terrace gravel deposits. We use the mode of the *a posteriori* slope values as the measured slope variable R_M in Equation 1 to calculate burial ages. We calculate burial age uncertainty at the 1σ range from the posterior

probability density functions for the regression slope, and analyze each result as R_M in Equation 1.

On each isochron we plot all ^{26}Al and ^{10}Be concentration data corresponding to the given site (Figure 3). We omit samples from regression analysis that have an ^{26}Al or ^{10}Be concentration or have an ^{26}Al/^{10}Be ratio that is one standard deviation greater or less than the mean of the respective parameter for the sample suite. We attribute outliers in the ^{26}Al or ^{10}Be concentration data to laboratory uncertainty (e.g., Ehrlanger et al., 2012) related to misestimation of ^{9}Be or ^{27}Al, or error in the AMS measurement of ^{10}Be or ^{26}Al. Outlier ^{26}Al/^{10}Be ratios occur for clasts with ^{26}Al concentrations depleted relative to ^{10}Be, reflecting previous cycles of burial and reworking, and resulting in a separate, much lower isotope concentration that skews the otherwise linear fit and violates the methodological assumption of an initial ^{10}Be/^{26}Al ratio resulting only from surface exposure.

4.3 Terrace Incision

We combine burial ages with lidar elevation data to calculate rates of incision on the Yakima River terraces. Terrace gravel burial ages provide a minimum age for the underlying strath, and correspond to a maximum incision rate (Bull, 1991; Burbank and Anderson, 2011; Hancock and Anderson, 2002). We assume that the Yakima River's modern graded channel profile matches the long-term equilibrium profile such that differencing the modern and paleo strath elevations provides a point measure of incision (e.g., Pazzaglia and Brandon, 2001).

We estimate strath height using a 1.5 m vertical resolution DEM derived from the 2008 GeoEarthScope Yakima lidar data (Figure 5). For a given terrace gravel, we extract point elevations along the mapped strath contact. We then subtract the modern river elevations at

corresponding profile distances to determine strath height. This difference provides strath height above the modern Yakima River water level. Since we are ultimately interested in bedrock incision, we also need to consider the thickness of the water and alluvium over the bedrock in the active channel. We account for these additional values by adding the corresponding measured terrace gravel thickness and the average estimated representative Yakima River channel depth of 1 m to each strath height, and use this approach to estimate total incision at each site (Figure S2). We calculate mean terrace incision and 1σ incision uncertainty based on the range of strath heights at each site, and determine time-averaged incision rates by normalizing mean strath height to the corresponding gravel burial age. We calculate incision rate uncertainty by propagating the 1σ strath height and burial age uncertainties in quadrature.

This approach to calculating time-averaged incision rates integrates all of the terrace-forming cycles that have occurred since the development of a given strath. Terraces across Manastash and Umtanum Ridge, also offer the opportunity to calculate interval rates between successive strath levels. Such rates span the interval between two geomorphically inset strath terraces, and reflect a period of vertical incision in response to some perturbation of base level, discharge, or sediment load. Because rivers spend a significant but often unknown period of time laterally eroding to create straths in between successive periods of incision (e.g., Bull, 1991; Hancock and Anderson, 2002), such interval rates may not be appropriately integrated over the entire cycle of lateral and vertical erosion during terrace formation. We calculate interval incision rates where geomorphically permissible by normalizing the difference between strath heights to the difference between corresponding burial ages, and propagating the 1σ uncertainties accordingly.

5. Yakima River terrace sample sites

5.1 Kittitas Valley

Miocene Columbia River Basalt Group and overlying Miocene upper Ellensburg Formation volcaniclastic rocks floor the broad Kittitas Valley (Figures 1, 2a-b, 4a). Pliocene Thorp Gravel caps this underlying bedrock, and is discontinuously overlain by Quaternary loess of the Palouse Formation (Porter, 1976; Waitt, 1979). Waitt (1979) interpreted the Thorp Gravel as outwash transported by the main stream of the ancestral Yakima River, forming the paleosurface of Kittitas Valley, and reports a fission track age of 3.64 ± 0.37 (1σ) Ma for a tephra in the Thorp Gravel at a site 25-30 km to the northwest of Potato Hill (see Table 1, Figures 1, 2, and 5 of Waitt, 1979). Bentley (1977) correlated the uppermost gravel at Potato Hill to the Thorp as mapped in the northwest part of the Kittitas Valley.

In the southern Kittitas Valley, Potato Hill (Figures 2b, 4b, S3) exposes stratigraphic relationships between the units in a ~10-m-deep gravel quarry cut into the side of a prominent, north sloping geomorphic surface (Figure 4b). This outcrop comprises a 1-2 m thick loess mantle over a 2-3-m-thick package of weakly cemented Thorp Gravel truncating north-dipping beds in the underlying Ellensburg Formation (Figures 4b, 5a). Underlying Ellensburg Formation beds dip up to ~10° to the north, while the surface of Potato Hill and the capping Thorp Gravel have lesser northward slopes of ~3-5°. The geometric relationship between Ellensburg and Thorp bedding is consistent with syntectonic deposition of the Thorp Gravel, and indicates progressive northward tilting in the basin north of Manastash Ridge starting before, or sometime after the deposition of the Ellensburg Formation (Bentley, 1977). We sampled the base of Bentley's (1977) inferred Thorp Gravel at Potato Hill (Figure S3) to assess a local burial age using the cosmogenic isochron method.

5.2 Manastash Ridge

The Manastash Ridge range front forms the southern boundary of the Kittitas Valley (Figures 2a-b, 4a), and is underlain by southwest-dipping range front reverse faults (Ladinsky, 2012) adjoined by the Thrall anticline (Figures 2a-b) (Bentley, 1977). A sequence of at least three strath terraces occupies the Manastash Ridge reach of the Yakima River canyon, each of which we sampled for isochron burial dating. We briefly describe each of the three sites below, two of which successfully yielded isochron burial ages.

On the east side of the Yakima River canyon entrance, the Manastash Ridge range front preserves the highest (~150 m above the channel) and most extensive strath terrace associated with the canyon. The terrace comprises a thick loess deposit mantling rounded basaltic cobbles that overly a basalt strath surface, all of which are exposed as float on the south flank of the terrace (Qg0, Figure 2b). We recovered Qg0 cobbles in a ~0.6 m thick deposit of angular to well-rounded, pebble to small cobble sized basalt clasts directly overlying basaltic bedrock at the base 1.2 m deep backhoe pit in the terrace. Unfortunately, the <2 m thickness of the deposit and the lack of quartz in the basaltic clasts did not permit isochron burial dating of the deposit.

The Yakima River exposes the core of the Manastash anticline in an abandoned meander mantled by colluvium, loess, and fan deposits (Figure 2b), where Ladinsky (2012) mapped six terrace levels and determined IRSL ages for loess above one Yakima River terrace gravel deposit. We mapped five strath terrace levels at this location, including three sites mapped and one site sampled by Ladinsky (2012), termed Toth Road and Rattlesnake Dance terrace, where we sampled the gravel deposits.

The Toth Road site exposes a 4-5 m thick gravel deposit (Qg2) overlain by fan deposits above the folded Columbia River basalt of the Thrall anticline 54-58 m above the active channel

(Figures 2b, 5b, S4). We mapped the strath contact as the upper extent of angular basalt clasts in rounded gravel, several m above the strath and ~3 m below the gravel terrace tread (Table 1) (Figure). Rattlesnake Dance terrace comprises a ~3 m thick gravel deposit (Qg3, Figures 2a-b, S5) overlain by ~3 m of loess and capping a basalt strath, positioned 19-21 m above the active channel, in the core of the Manastash anticline (Figures 2b, 5c). The modern Yakima River terrace (Qg4, Figure 2a-b) sits roughly 18 m below the Rattlesnake Dance terrace (Figure 5c).

5.3 Manastash-Umtanum syncline

The Yakima River incises a cutoff meander in the syncline between the Manastash and Umtanum Ridge anticlines (Figures 2c, S6). At this site, described here as Meander Terrace, we mapped three geomorphically related gravel deposits (Qg1c-d) capping basalt straths at two distinct levels, nearly continuously covered by several meters of loess and basaltic colluvium shed from the steep abandoned meander walls (Figure 2c). We sampled the lowest gravel deposit at this site directly above the strath and ~2 m below the top of the gravel (Figure S6).

5.4 Umtanum Ridge

Four levels of unpaired strath terraces occur where the Yakima River incises across Umtanum Ridge (Figures 2, 3). We sampled for ^{26}Al-^{10}Be isochron burial dating at four sites spanning this reach. The two highest strath terrace sites that we sampled in the canyon are among the four along this reach, informally named the Lower and Higher Island terraces (Figures 2c, 3, S6). The Island terraces are positioned on the forelimb of Umtanum Ridge near the location of several mapped, north-dipping thrust splays (Figure 2a, c), and therefore occupy a structural high despite their location several km upstream of the anticlinal axis.

The site that we term Lower Island terrace comprises a ≤4 m thick gravel deposit (Qg1b) capping a well-exposed basalt strath positioned 56-60 m above the active channel (Figures 2c, 5e, S8a-b, S9). We sampled the gravel ~1 m above the strath and 2-3 m below the top of the gravel. A highway road cut through the Lower Island terrace exposes the gravel-over-basalt strath relationship, as well as a thick (3-4 m) package of horizontally bedded, fine-grained, white- to brown- colored sediment overlying the gravel (Figure S8a-b). This sedimentary package also includes possible paleosols and lacustrine diatomites interfingered with colluvium stringers that pinch out to the south. Given this sequence, and the spatial regularity of landsliding in the Canyon (Figure 2a), we speculate that this package may represent deposition over the previously developed strath terrace in a landslide-dammed lake. The entire exposure is uniformly capped by a thick (~50 cm) brown soil that follows the topographic surface.

The Lower Island terrace is directly inset ~20-30 below the site we term Higher Island terrace. The Higher Island site comprises a 4-5 m thick gravel deposit (Qg1a) capping a well-exposed strath positioned 92-98 m above the active channel, and preserves a broad, intact tread (Figures 2c, 5e, S10). We sampled the gravel in a hand-dug pit directly over the strath, 3-5 m below the deposit tread, but only 1.9 to 1.7 m below the sloping surface of the gravel riser.

The site that we term Death Chute terrace corresponds with the deepest section of the Yakima River Canyon in the core of the Umtanum Ridge anticline. At this site, a prominent road cut exposes a ≤5 m thick gravel deposit (Qg2) capping a well-exposed basalt strath positioned 29-31 m above the active channel (Figures 2a, 2d, 5f, S11). The basalt strath in this location is strongly fractured (Figure S7a), likely related to its location between two exposed thrust faults (Figure 2d). We sampled the gravel directly over the strath and ~4 m below the top of the gravel.

The geomorphically lowest deposit we sampled, termed the Big Pines terrace, occurs ~5-8 m above the Yakima River on the backlimb of Umtanum Ridge (Figures 2d, 5g, S12). The Big Pines terrace comprises a 6 m thick gravel deposit (Qg3) capping a basalt strath positioned ≤3 m above the active channel (Figure 5g), and features an intact tread mantled by a thin (10-20 cm) rocky light brown soil truncating prominent massive south-dipping internal beds (Figure S6b). We sampled the gravel ~2 m above the strath and 4 m below the deposit tread for ^{26}Al-^{10}Be isochron burial ages.

6. Results

In this section, we report ^{26}Al-^{10}Be isochron burial ages summarized in Table 2 and calculated based on cosmogenic isotope data reported in Table S1. Of the 40 samples we analyze to determine burial ages, 10 were sampled and measured by Coppersmith et al. (2014) (Table S1). We also report total strath incision, and time-averaged incision rates for each site based on the gravel burial ages and strath incision estimates. In general, terrace gravel burial ages range from zero to ~2.9 m.y., strath incision ranges from ~3 to ~98 m, and incision rates are up to ~0.07 mm/yr. We also report interval incision rates between geomorphically inset sites that generally agree with time-averaged rates. All quoted uncertainties are 1 σ.

6.1 Potato Hill, Kittitas Valley

Potato Hill samples (n = 3) fit a line (slope = 1.67 ± 0.09, R^2 = 0.98) that implies a burial age of 2.9 ± 0.1 Ma for the Thorp Gravel (Figure 3a). Despite being ~0.7 m.y. younger, the burial age is consistent with Waitt's (1979) zircon fission track age of 3.64 ± 0.37 (1σ) Ma for tephras in the Thorp Gravel for several reasons. Potato Hill is ~25-35 km downstream of Waitt's (1979) sample sites, and hence permissibly younger. Also, the absence of tephras in the Thorp

Gravel at Potato Hill suggests local strath formation and gravel deposition after emplacement of the dated tephras. Based on gravel thickness (~3 m) and strath height (15-19 m), the burial age corresponds to an incision rate of <0.01 mm/yr for the past 2.8-3.0 m.y. in the southern Kittitas Valley.

6.2 Manastash Ridge

Toth Road samples (n = 5) yield an isochron (slope = 4.15 ± 0.44, R^2 = 0.95) burial age of 1.1 ± 0.1 Ma for the gravel (Figure 3b). Based on gravel thickness (~5 m) and strath height (54-58 m), the burial age corresponds to an average incision rate of 0.05 ± 0.005 mm/yr for the past 1.0-1.2 m.y.

Isochron analysis of the Rattlesnake Dance terrace samples (n = 5, slope = 5.83 ± 0.45, R^2 = 0.91) implies a burial age of 0.3 ± 0.1 Ma for the gravel (Figure 3c), stratigraphically consistent with Ladinsky's (2012) IRSL age of 84.2-93.3 ka for the overlying loess, and very near the nominal ~0.2 Ma lower age limit of the isochron burial method (Balco and Rovey, 2008). Based on gravel thickness (~3 m) and strath height (19-21 m), the burial age corresponds to fluvial downcutting at an average incision rate of 0.07 ± 0.02 mm/yr over the past ~200-400 ky. Rattlesnake Dance terrace is inset 36 ± 2 m lower than the ~1.1 Ma Toth Road terrace (Figure 2b), suggesting interval incision rates of 0.04 ± 0.01 mm/yr over the 0.8 ± 0.2 m.y. period between formation of these surfaces.

6.3 Manastash-Umtanum syncline

Meander Terrace samples (n = 5) have a linear fit (slope = 5.83 ± 0.34, R^2 = 0.91) that corresponds with a burial age of 1.6 ± 0.1 Ma for the gravel (Figure 3d). Based on gravel

thickness (~2 m) and strath height (10-12 m), the burial age corresponds to an average incision

rate of 0.007 mm/yr for the past 1.5-1.7 m.y.

6.4 Umtanum Ridge

Isochron analysis of Lower Island samples (n = 4, slope = 3.21 ± 0.40, R^2 = 0.98) implies

a burial age of 1.6 ± 0.1 Ma for the gravel (Figure 3f). Based on gravel thickness (~4 m) and

strath height (56-60 m), the burial age corresponds to an average incision rate of 0.04 ± 0.003

mm/yr for the past 1.5-1.7 m.y.

Higher Island samples (n = 6, slope = 6.96 ± 1.14, R^2 = 0.67) yield an isochron burial age

of zero for the gravel (Figure 3e). The zero age is incompatible with the age limit imposed by the

~1.6 Ma Lower Island terrace that is directly inset 37 ± 4 m below the Higher Island terrace

(Figure 5e). We attribute the zero age to the narrow range of ^{10}Be concentrations measured in

these samples (6.10 x 10^4 ± 2.93 x 10^3 to 7.17 x 10^4 ± 2.93 x 10^3 atoms/g), which most likely

reflects a large amounts of post-burial production of the cosmogenic nuclide. Such an

explanation is consistent with the shallow depth of the samples (1.9 m below the surface) and the

age of the deposit (>1.6 Ma).

Isochron analysis of Death Chute samples (n=5) yields a slope well below the production

ratio (slope = 4.30 ± 0.43, R^2 = 0.84) and implies a burial age of 0.9 ± 0.1 Ma for the gravel

(Figure 3g). Based on gravel thickness (~5 m) and strath height (29-31 m), the burial age

corresponds to an average incision rate of 0.03 ± 0.004 mm/yr for the past 0.8-1.0 m.y. The

Death Chute terrace is geomorphically inset 29 ± 4 m to the Lower Island terrace several km

downstream (Figures 2a, c-d), permitting incision during the 0.7 ± 0.2 m.y. interval between the

terraces at 0.04 ± 0.01 mm/yr.

Big Pines samples (n = 3, slope = 6.75 ± 0.13, $R^2 = 0.85$) imply an isochron burial age of 0.0 ± 0.2 Ma for the gravel (Figure 3h). The deposit age cannot be less than zero, so we truncate the negative error. We consider the upper limit burial age (0.2 Ma) for calculating a minimum incision rate. Based on gravel thickness (6 m) and strath height (≤ 3 m), the maximum burial age permits a minimum incision rate of 0.01 ± 0.01 mm/yr for the past 0.2 m.y.

7. Discussion

The distribution and age of terrace gravels (~0.3 to ~2.9 Ma) between the southern Kittitas Valley and Umtanum Ridge (Figures 6a-c) constrains the history of fluvial incision of the Yakima River and therefore differential rock uplift since the Middle Pleistocene (Figures 7a-b). Equating strath terrace incision with rates of rock uplift relies on the assumption that the modern river channel represents an equilibrium profile that is stable over geologic time (e.g., Lavé and Avouac, 2001; Pazzaglia and Brandon, 2001). We make this assumption based on the observation that the Yakima River maintains a graded channel free of prominent knickpoints from the alluvial Kittitas Valley through the basalt-floored Yakima River Canyon (Figure 6b).

In order to calculate rock uplift in the canyon, we need to consider the background rate of base level lowering from calculated incision rates. Similar incision rates in both the Kittitas Valley (~0.01 mm/yr) and the Umtanum-Manastash syncline (~0.01 mm/yr) within the canyon suggest that the background base level rate is similar within and outside the canyon over the past ~2.9 m.y. We therefore equate the full incision rate at each terrace to time-averaged rock uplift resulting from the vertical component of the underlying faulting and folding.

The distribution of terrace gravels and ages in the Yakima River Canyon also provides insight into the spatial pattern of Quaternary deformation across the Manastash and Umtanum

Ridges. Profile comparisons of topography and bedrock structure (Figure 6a) with the location of remnant terrace gravels (Figure 6b), and ages (Figure 6c) show that the Manastash and Umtanum Ridge anticlines preserve substantially more terrace remnants and levels than the intervening syncline (Figure 6a-b), likely as a result of the attendant differential rock uplift in the anticlines relative to the synclines. For example, the synclinal Qg1 deposit at Meander terrace is positioned only 12-14 m above the channel, whereas Qg1 deposits occur up to ~98 m above the channel at Higher Island terrace in the Umtanum Ridge anticline (Figure 6b). Accordingly, the fastest time-averaged canyon incision rates come from strath terraces in the Manastash and Umtanum anticlines (0.04 ± 0.1 mm/yr), and the lowest rate from Meander terrace in the Manastash-Umtanum syncline (<0.01 mm/yr) (Figure 7a-b).

Spatial variations in bedrock incision rate and channel narrowing are consistent with expectations of fluvial response to differential rock uplift on the Yakima River across the Manastash and Umtanum Ridge structures. Incision rates along the Yakima River Canyon correspond spatially with changes in channel width (Figure 7b). The Yakima River channel maintains relatively constant slope through the canyon (Figure 6b), but narrows across Manastash and Umtanum anticlines (Fisher et al., 2013) in conjunction with the high incision rates and also with the daylighting reverse fault at the mouth of the canyon (Figure 7b). The zones of channel narrowing do not correspond to large debris flows or other point sources of coarse sediment in the canyon. Several studies demonstrate that channel width changes can occur across zones of active differential uplift without concomitant channel steepening or preservation of knickpoints (e.g., Lave and Avouac, 2001; Amos and Burbank, 2007). Based on the spatial overlap between modern channel narrowing and relatively high bedrock incision rates over ~1-2

m.y., we infer that both the Yakima River channel geometry and the spatial incision rate distribution represent long-term features of Yakima River channel response to tectonic forcing.

Comparing time-averaged incision rates for each terrace with incision rates between inset terrace levels, the time-averaged rates range up to 0.06 and 0.09 mm/yr on Manastash and Umtanum Ridge anticlines, respectively, while corresponding interval rates between Toth and Rattlesnake Dance terraces, and between the Lower Island and Death Chute terraces range up to 0.05 mm/yr. The general agreement between time-averaged and interval incision rates suggests that, where the Yakima River cuts across the Manastash and Umtanum Ridge anticlines, differential rock uplift and incision rates have been stable within a factor of <2 since ~1.6 Ma.

Whether faulting or folding primarily drives differential rock uplift on the Manastash and Umtanum Ridge structures and Yakima fold belt deformation in general remains unknown. Deformed terraces have been used to infer the geometric and kinematics of thrust- related folds in a variety of regions (e.g., Rockwell et al., 1988; Lave and Avouac. 2001; Amos et al., 2007). Such inferences, however, require intact and relatively continuous treads, not the relatively sparse treads preserved on the Yakima River terraces. Instead, we explore the deformation rates implied by our incision rate data using a simple geometric model of folding and rock uplift in the Yakima fold belt controlled by slip on underlying master thrust faults (e.g., Blakely et al., 2011; Reidel, 1984, West et al., 1996) general enough to be consistent with either the fault-propagation (Suppe and Medwedeff, 1990) or fault-bend model (Casale and Pratt, 2015; Suppe, 1983).

We evoke a simple 2D model to relate time-averaged rock uplift rates on Manastash and Umtanum Ridge to rates of shortening associated with reverse slip on master fault planes underlying each fold (Figure 8). We use the average calculated strath terrace incision rates corresponding with zones of channel narrowing (Figure 7b) to assign rock uplift rates across

Manastash (average of Toth Road and Rattlesnake Dance terrace, 0.06 ± 0.02 mm/yr) and Umtanum Ridge (Lower Island terrace, 0.04 ± 0.003 mm/yr). We use the geometric relationships between rock uplift rate and master faults that dip ~30° south (Ladinsky, 2012; Miller, 2014), adding conservative fault dip uncertainties of ±10°, to calculate a range of hypothetical shortening rates (Figure 8).

This simple model estimates average horizontal shortening at rates of 0.12 ± 0.08 and 0.08 ± 0.03 mm/yr respectively spanning up to 0.4 and 1.6 m.y. on faults beneath Manastash and Umtanum Ridge. The combined Manastash and Umtanum Ridge shortening rates account for a relatively small fraction of the modern, geodetically inferred shortening across the fold belt (1.9 ± 0.5 mm/yr, McCaffrey et al., 2013). It is possible that both the modern geodetic rates and the Manastash and Umtanum shortening rates apply to longer-term (~10.5 m.y.) geologic deformation across the fold belt. If true, then active deformation on other Yakima fold belt structures occurs over the long term at rates equivalent to or faster than the Manastash and Umtanum Ridge anticlines.

Given the comparative lack of information on Yakima folds and faults other than Manastash and Umtanum, it remains unclear which structures take up the remaining active contraction. Nonetheless, the Manastash and Umtanum Ridge anticlines and underlying reverse faults are actively deforming at modest rates, and pose a seismic hazard given the $M_w>7$ seismic potential of the related faults (Blakeley et al., 2011; Wells and Coppersmith, 1994). The relative lack of information about the remaining potentially active structures, which include 12 fault-related folds (e.g., Reidel, 1984) and a number of right lateral strike-slip faults (Anderson et al., 2013), results in considerable uncertainty surrounding the seismic hazard of individual structures within the Yakima fold belt.

Measured incision rates also place constraints on the age of the Yakima River Canyon (Figure 2). We extrapolate the time-averaged rate of downcutting to consider the timespan necessary to erode the total canyon depth across reconstructed (pre-erosion) structural-topographic highs at Manastash and Umtanum Ridge anticlines. Ladinsky's (2012) structural reconstruction places the Manastash anticline crest, developed in the ~14.1 Ma Wanapum basalt horizon, roughly 730 m above the modern Yakima River channel. Incising this depth at a steady average rate of ~0.07 mm/yr, as determined for the ~0.3 Ma Rattlesnake Dance terrace, requires ~10.4 m.y. The relatively young Rattlesnake Dance terrace represents only a small fraction of the total canyon depth, so the corresponding young age likely represents a short interval of the total incision duration. As such, extrapolating a longer temporal record of canyon incision should better reflect the total time required to cut the canyon.

The ~1.6 Ma Lower Island terrace gravel on the Umtanum Ridge forelimb provides the longest record of time-averaged canyon incision, at a rate of ~0.04 mm/yr. Miller's (2014) structural reconstruction places the crest of the Umtanum anticline, developed in ~15.7 Ma Grand Ronde basalt, roughly 640 m above the modern Yakima River channel. Incising this depth at a steady average rate of ~0.04 mm/yr requires ~16.0 m.y. Given the consistency between these comparatively long- and short-term time-averaged incision rates, modern canyon morphology reflects downcutting that started well prior to the Quaternary.

8. Conclusions

We mapped and dated strath terraces in the Yakima River Canyon, and calculated bedrock incision rates spanning Manastash and Umtanum Ridge structures. Bayesian regression and cosmogenic ^{26}Al-^{10}Be isochron analysis provided burial ages of Cascade-derived, strath-

capping gravels in the Yakima River Canyon, characterizing four intervals of terrace formation

spanning 0.2-0.4 Ma (Qg3), 0.8-1.2 Ma (Qg2), 1.5-1.9 Ma (Qg1), and 2.8-3.0 Ma (Thorp). In

combination with our mapping, lidar data indicate that strath elevations range up to ~150 m

above the active channel with the highest strath terraces exposed in anticlinal forelimbs and

lower terraces within synclines. Time-averaged bedrock incision rates, derived from ^{26}Al-^{10}Be

isochron burial ages and strath heights, are <0.01 mm/yr outside the canyon and in the

Manastash-Umtanum syncline, while anticlinal incision rates are an order of magnitude higher

(~0.02 – 0.07 mm/yr), with the highest rates corresponding to zones of channel narrowing.

Interval incision rates calculated between geomorphically inset terraces compare well with the

time-averaged rates. Extrapolating these rates suggests the canyon has been a feature on the

landscape since well before Quaternary time.

Collectively these results demonstrate that differential bedrock incision continued at

relatively steady average rates through the Quaternary. The spatial distribution of differential

uplift and the relatively uniform basaltic bedrock allow us to equate bedrock incision to uplift.

We estimate horizontal shortening on the Manastash and Umtanum Ridges based on the

assumption that both folds verge in the direction of faulting at depth (dipping ~20 to 40° south).

We estimate time-averaged shortening at ~0.12 to ~0.08 mm/yr across Manastash and Umtanum

Ridge, respectively, suggesting that these structures take up only a fraction of the contemporary

geodetic shortening rate (1.9 ± 0.5 mm/yr, McCaffrey et al., 2013). These results provide the first

quantitative estimates of active Quaternary deformation in the Yakima fold belt, and suggest that

other structures in the region actively accommodate the remaining geodetic strain. It remains

unclear which of the other Yakima folds and faults are active, highlighting the need for further

geologic investigations of the tectonic structures and associated seismic hazard across central

Washington.

9. References Cited

Amos, C. B., and Burbank, D. W., 2007, Channel width response to differential uplift: Journal of Geophysical Research: Earth Surface (2003–2012), v. 112, no. F2. doi:02010.01029/02006JF000672.

Amos, C. B., Burbank, D. W., Nobes, D. C., and Read, S. A. L., 2007, Geomorphic constraints on listric thrust faulting: Implications for active deformation in the Mackenzie Basin, South Island, New Zealand: Journal of Geophysical Research: Solid Earth (1978–2012), v. 112, no. B3. doi:10.1029/2006JB004291.

Anderson, J. L., Tolan, T. L., and Wells, R. E., 2013, Strike-slip faults in the western Columbia River flood basalt province, Oregon and Washington. Geological Society of America Special Papers, no. 497, p. 325-347. doi: 10.1130/2013.2497(13).

Balco, G., and Rovey, C. W., 2008, An isochron method for cosmogenic-nuclide dating of buried soils and sediments: American Journal of Science, v. 308, no. 10, p. 1083-1114. doi: 10.2475/10.2008.02.

Bentley, R. D., 1977, Stratigraphy of the Yakima basalts and structural evolution of the Yakima ridges in the western Columbia Plateau, in Brown, E. H., and Ellis, R. C., eds., Geological Excursions in the Pacific Northwest: Western Washington University, Published as a geology field guide in conjunction with the 1977 annual meeting of the Geological Society of America, p. 51.

Bingham, J. W., and Grolier, M. J., 1966, The Yakima basalt and Ellensburg formation of south-central Washington. US Government Printing Office. http://pubs.usgs.gov/bul/1224g/report.pdf

Blakely, R. J., Sherrod, B. L., Weaver, C. S., Rohay, A. C., and Wells, R. E., 2012, Tectonic Setting of the Wooded Island Earthquake Swarm, Eastern Washington: Bulletin of the Seismological Society of America, v. 102, no. 4, p. 1786-1795. doi: 10.1785/0120110189.

Blakely, R. J., Sherrod, B. L., Weaver, C. S., Wells, R. E., and Rohay, A. C., 2014, The Wallula fault and tectonic framework of south-central Washington, as interpreted from magnetic and gravity anomalies: Tectonophysics, no. 624, p. 32-45. doi: 10.1016/j.tecto.2013.11.006.

Blakely, R. J., Sherrod, B. L., Weaver, C. S., Wells, R. E., Rohay, A. C., Barnett, E. A., and Knepprath, N. E., 2011, Connecting the Yakima fold and thrust belt to active faults in the Puget Lowland, Washington: Journal of Geophysical Research, v. 116, no. B7. doi: 10.1029/2010JB008091.

Blakely, R. J., Wells, R. E., Weaver, C. S., and Johnson, S. Y., 2002, Location, structure, and seismicity of the Seattle fault zone, Washington: Evidence from aeromagnetic anomalies, geologic mapping, and seismic-reflection data.: Geological Society of America Bulletin, v. 114, no. 2, p. 169-177. doi: 10.1130/0016-7606(2002)114<0169:LSASOT>2.0.CO;2.

Bretz, J. H., 1969, The Lake Missoula floods and the channeled scabland: The Journal of Geology, p. 505-543. doi: 10.1086/627452.

Bull, W. B., 1991, Geomorphic responses to climatic change, New York, Oxford University Press, 326 p. OSTI: 5603696

Burbank, D. W., and Anderson, R. S., 2011, Tectonic Geomorphology, John Wiley & Sons. doi: 10.1002/9781444345063.

Campbell, N. P., and Bentley, R. D., 1981, Late Quaternary deformation of the Toppenish Ridge uplift in south-central Washington: Geology, v. 9, no. 11, p. 519. doi: 10.1130/0091-7613(1981)9<519:LQDOTT>2.0.CO;2.

Casale, G., and Pratt., T. L., 2015, Thin- or thick-skinned faulting in the Yakima Fold and Thrust Belt (WA)? Constraints from kinematic modeling of the Saddle Mountains anticline: Bulletin of the Seismological Society of America, doi:10.1785/0120140050.

Chmeleff, J., von Blanckenburg, F., Kossert, K., & Jakob, D., 2010, Determination of the 10 Be half-life by multicollector ICP-MS and liquid scintillation counting. Nuclear Instruments and Methods in Physics Research Section B: Beam Interactions with Materials and Atoms, v. 268, no. 2, p. 192-199. doi:10.1016/j.nimb.2009.09.012

Çiner, A., Doğan, U., Yıldırım, C., Akçar, N., Ivy-Ochs, S., Alfimov, V., Kubik, P. W., and Schlüchter, C., 2015, Quaternary uplift rates of the Central Anatolian Plateau, Turkey: insights from cosmogenic isochron-burial nuclide dating of the Kızılırmak River terraces: Quaternary Science Reviews,, v. 107, no. 81-97. doi: 10.1016/j.quascirev.2014.10.007.

Corbett, L. B., Young, N. E., Bierman, P. R., Briner, J. P., Neumann, T. A., Rood, D. H., and Graly, J. A., 2011, Paired bedrock and boulder 10 Be concentrations resulting from early Holocene ice retreat near Jakobshavn Isfjord, western Greenland. Quaternary Science Reviews, v. 30, no. 13, p. 1739-1749. doi:10.1016/j.quascirev.2011.04.001

Coppersmith K.J., Bommer, J.J., Hanson, K.L., Unruh, J., Coppersmith, R.T., Wolf, L., Youngs, R., Rodriguez-Marek, A., Al Atik, L., Toro, G., Montaldo-Falero, V., 2014. Hanford Sitewide Probabilistic Seismic Hazard Analysis. PNNL-23361, Pacific Northwest National Laboratory, Richland Washington. http://www.hanford.gov/page.cfm/Official Documents/HSPSHA

D'Agostini, Giulio, 2003, Bayesian reasoning in data analysis. World Scientific. http://dx.doi.org/10.1142/5262

-, 2005, Fits, and especially linear fits, with errors on both axes, extra variance of the data points and other complications. arXiv preprint physics/0511182.

Darling, A. L., Karlstrom, K. E., Granger, D. E., Aslan, A., Kirby, E., Ouimet, W. B., Lazear, G. D., Coblentz, D. D., and Cole, R. D., 2014. New incision rates along the Colorado River system based on cosmogenic burial dating of terraces: Implications for regional controls on Quaternary incision." Geosphere: GES00724-1. doi:10.1130/GES00724.1

Duvall, A., Kirby, E., and Burbank, D., 2004. Tectonic and lithologic controls on bedrock channel profiles and processes in coastal California. Journal of Geophysical Research: Earth Surface (2003–2012), v. 109 no. F3. doi:10.1029/2003JF000086

Erlanger, E. D., Granger, D. E., and Gibbon, R. J., 2012, Rock uplift rates in South Africa from isochron burial dating of fluvial and marine terraces: Geology, v. 40, no. 11, p. 1019-1022. doi: 10.1130/G33172.1.

Fisher, G. B., Bookhagen, B., and Amos, C. B., 2013, Channel planform geometry and slopes from freely available high-spatial resolution imagery and DEM fusion: Implications for channel width scalings, erosion proxies, and fluvial signatures in tectonically active landscapes: Geomorphology, v. 194, p. 46-56. doi: 10.1016/j.geomorph.2013.04.011.

Gomberg, J., Sherrod, B., Trautman, M., Burns, E., and Snyder, D., 2012, Contemporary Seismicity in and around the Yakima Fold-and-Thrust Belt in Eastern Washington: Bulletin of the Seismological Society of America, v. 102, no. 1, p. 309-320. doi: 10.1785/0120110065.

Granger, D. E. (2006). A review of burial dating methods using 26Al and 10Be.Geological Society of America Special Papers, 415, 1-16. doi: 10.1130/2006.2415(01).

Hancock, G. S., and Anderson, R. S., 2002, Numerical modeling of fluvial strath-terrace formation in response to oscillating climate: Geological Society of America Bulletin, v. 114, no. 9, p. 1131-1142. doi: 10.1130/0016-7606(2002)114<1131:NMOFST>2.0.CO;2

Hooper, P. R., and Conrey, R. M., 1989, A model for the tectonic setting of the Columbia River basalt eruptions: Geological Society of America Special Papers, v. 239, no. 293-306.

Johnson, S. Y., Dadisman, S. V., Childs, J. R., and Stanley, W. D., 1999, Active tectonics of the Seattle fault and central Puget Sound, Washington—Implications for earthquake hazards.: Geological Society of America Bulletin, v. 111, no. 7, p. 1042-1053. doi: 10.1130/0016-7606(1999)111<1042:ATOTSF>2.3.CO;2.

Johnson, S. Y., Potter, C. J., Miller, J. J., Armentrout, J. M., Finn, C., and Weaver, C. S., 1996, The southern Whidbey Island fault: an active structure in the Puget Lowland, Washington.: Geological Society of America Bulletin, v. 108, no. 3, p. 334-354. doi: 10.1130/0016-7606(1996)108<0334:TSWIFA>2.3.CO;2.

Kelsey, H. M., Sherrod, B. L., Blakely, R. J., and Haugerud, R. A., 2012, Holocene faulting in the Bellingham forearc basin: Upper‐plate deformation at the northern end of the Cascadia subduction zone.: Journal of Geophysical Research: Solid Earth (1978–2012), v. 117, no. B3. doi: 10.1029/2011JB008816.

Kelsey, H. M., Sherrod, B. L., Nelson, A. R., and Brocher, T. M., 2008, Earthquakes generated from bedding plane-parallel reverse faults above an active wedge thrust, Seattle fault zone: Geological Society of America Bulletin, v. 120, no. 11-12, p. 1581-1597. doi: 10.1130/B26282.1.

Ladinsky, T. C., 2012, Late Quaternary evolution of the Manastash anticline and Manastash range front, Yakima fold belt, Washington: Influence of tectonics and climate [MS Thesis]: Humboldt State University, 95 p. URI: http://hdl.handle.net/2148/1251

Lavé, J., and Avouac, J. P., 2001, Fluvial incision and tectonic uplift across the Himalayas of central Nepal: Journal of Geophysical Research, v. 106, no. B11, p. 26561. doi: 10.1029/2001JB000359.

McCaffrey, R., King, R. W., Payne, S. J., and Lancaster, M., 2013, Active tectonics of northwestern U.S. inferred from GPS-derived surface velocities: Journal of Geophysical Research: Solid Earth, v. 118, no. 2, p. 709-723. doi: 10.1029/2012JB009473.

Miller, B. A., 2014, On the origin of Umtanum Ridge: kinematics of Neogene slip [MS Thesis]: University of Washington. http://hdl.handle.net/1773/25333

Muzikar, P., 2011, Geological constraints and 26Al–10Be burial dating isochrons: Earth Surface Processes and Landforms, v. 36, no. 7, p. 946-952. doi: 10.1002/esp.2124.

Nelson, A. R., Johnson, S. Y., Kelsey, H. M., Wells, R. E., Sherrod, B. L., Pezzopane, S. K., Bradley, L.-A., Koehler, R. D., and Bucknam, R. C., 2003, Late Holocene earthquakes on the Toe Jam Hill fault, Seattle fault zone, Bainbridge Island, Washington.: Geological Society of America Bulletin, v. 115, no. 11, p. 1388-1403. doi: 10.1130/B25262.1.

Nishiizumi, K., 2004, Preparation of 26 Al AMS standards: Nuclear Instruments and Methods in Physics Research Section B: Beam Interactions with Materials and Atoms, v. 223, p. 388-392. doi: 10.1016/j.nimb.2004.04.075.

Nishiizumi, K., Imamura, M., Caffee, M. W., Southon, J. R., Finkel, R. C., & McAninch, J.,

2007, Absolute calibration of 10 Be AMS standards. Nuclear Instruments and Methods in Physics Research Section B: Beam Interactions with Materials and Atoms, v. 258, no. 2, p. 403-413. doi:10.1016/j.nimb.2007.01.297.

Pazzaglia, F. J., and Brandon, M. T., 2001, A fluvial record of long-term steady-state uplift and erosion across the Cascadia forearc high, western Washington State. American Journal of Science, v. 301, no. 4-5, p. 385-431. doi: 10.2475/ajs.301.4-5.385.

Petersen, M. D., Moschetti, M. P., Powers, P. M., Mueller, C. S., Haller, K. M., Frankel, A. D., Zeng, Y., Rezaeian, S., Harmsen, S. C., Boyd, O. S., Field, N., Chen, R., Rukstales, K. S., Luco, N., Wheeler, R. L., Williams, R. A., and Olsen, A. H., 2014, Documentation for the 2014 update of the United States national seismic hazard maps: U.S. Geological Survey Open-File Report 2014–1091, in doi , ed., p. 243. doi: 10.3133/ofr20141091.

Porter, S. C., 1975, Weathering rinds as a relative-age criterion: Application to subdivision of glacial deposits in the Cascade Range: Geology, v. 3, no. 3, p. 101. doi: 10.1130/0091-7613(1975)3<101:WRAARC>2.0.CO;2.

-, 1976, Pleistocene glaciation in the southern part of the North Cascade Range, Washington: Geological Society of America Bulletin, v. 87, no. 1, p. 61. doi: 10.1130/0016-7606(1976)87<61:PGITSP>2.0.CO;2.

Pratt, T. L., 2012, Large-scale splay faults on a strike-slip fault system: The Yakima Folds, Washington State: Geochemistry, Geophysics, Geosystems, v. 13, no. 11. doi:10.1029/2012GC004405.

Raisz, E., 1945, The Olympic-Wallowa Lineament: Abstracts of Proc. Sess., no. 1364, p. 42-43.

Reidel, S. P., 1984, The Saddle Mountains; the evolution of an anticline in the Yakima fold belt: American Journal of Science, v. 284, no. 8, p. 942-978. doi: 10.2475/ajs.284.8.942.

Russell, I. C., 1893, A geological reconnoissance in Central Washington, US Government Printing Office.

Saltus, R. W., 1993, Upper-crustal structure beneath the Columbia River Basalt Group, Washington: Gravity interpretation controlled by borehole and seismic studies: Geological Society of America Bulletin, v. 105, no. 9, p. 1247-1259. doi: 10.1130/0016-7606(1993)105<1247:UCSBTC>2.3.CO;2.

Sherrod, B. L., Barnett, E., Schermer, E., Kelsey, H. M., Hughes, J., Foit, F. F., Weaver, C. S., Haugerud, R., and Hyatt, T., 2013, Holocene tectonics and fault reactivation in the foothills of the north Cascade Mountains, Washington: Geosphere, v. GES00880-1. doi: 10.1130/GES01067.1.

Sherrod, B. L., Blakely, R. J., Weaver, C. S., Kelsey, H. M., Barnett, E., Liberty, L., Meagher, K. L., and Pape, K., 2008, Finding concealed active faults: Extending the southern Whidbey Island fault across the Puget Lowland, Washington: Journal of Geophysical Research: Solid Earth (1978–2012), v. 113, no. B5. doi: 10.1029/2007JB005060.

Sherrod, B. L., Brocher, T. M., Weaver, C. S., Bucknam, R. C., Blakely, R. J., Kelsey, H. M., Nelson, A. R., and Haugerud, R., 2004, Holocene fault scarps near Tacoma, Washington, USA: Geology, v. 32, no. 1, p. 9-12. doi: 10.1130/G19914.1.

Smith, G. A., 1988, Neogene synvolcanic and syntectonic sedimentation in central Washington: Geological Society of America Bulletin, v. 100, no. 9, p. 1479-1492. doi: 10.1130/0016-7606(1988)100<1479:NSASSI>2.3.CO;2.

Smith, G. O., 1903, Anticlinal mountain ridges in central Washington: The Journal of Geology, v. 11, no. 2, p. 166-177. doi: 10.1086/621067.

Suppe, J., 1983, Geometry and kinematics of fault-bend folding: American Journal of Science, p. 684-721. doi: 10.2475/ajs.283.7.684.

Waitt, R. B., 1980, About forty last-glacial Lake Missoula jökulhlaups through southern Washington: The Journal of Geology, p. 653-679. doi: 10.1086/628553.

-, 1985, Case for periodic, colossal jökulhlaups from Pleistocene glacial Lake Missoula: Geological Society of America Bulletin, v. 96, no. 10, p. 1271-1286. doi: 10.1130/0016-7606(1985)96<1271:CFPCJF>2.0.CO;2.

Waitt, R. B., Jr., 1979, Late Cenozoic deposits, landforms, stratigraphy, and tectonism in Kittitas Valley, Washington.: U.S. Geological Survey. http://pubs.usgs.gov/pp/1127/report.pdf

Watters, T. R., 1988, Wrinkle ridge assemblages on the terrestrial planets: Journal of Geophysical Research: Solid Earth (1978-2012), v. 93, no. B9, p. 10236-10254. doi: 10.1029/JB093iB09p10236.

-, 1989, Periodically spaced anticlines of the Columbia plateau: Geological Society of America Special Papers, v. 239, p. 283-292. doi: 10.1130/SPE239-p283.

Wells, D. L., and Coppersmith, K. J., 1994, New empirical relationships among magnitude, rupture length, rupture width, rupture area, and surface displacement. Bulletin of the Seismological Society of America, v. 84, no. 4, p. 974-1002.

Wells, R. E., and McCaffrey, R., 2013, Steady rotation of the Cascade arc: Geology, v. 41, no. 9, p. 1027-1030. doi: 10.1130/G34514.1.

Wells, R. E., Weaver, C. S., and Blakely, R. J., 1998, Fore-arc migration in Cascadia and its neotectonic significance: Geology, v. 26, no. 8, p. 759. doi: 10.1130/0091-7613(1998)026<0759:FAMICA>2.3.CO;2.

West, M. W., Ashland, F. X., Busacca, A. J., Berger, G. W., and Shaffer, M. E., 1996, Late Quaternary deformation, Saddle Mountains anticline, south-central Washington: Geology, v. 24, no. 12, p. 1123. doi: 10.1130/0091-7613(1996)024<1123:LQDSMA>2.3.CO;2.

Wicks, C., Thelen, W., Weaver, C., Gomberg, J., Rohay, A., and Bodin, P., 2011, InSAR observations of aseismic slip associated with an earthquake swarm in the Columbia River flood basalts: Journal of Geophysical Research: Solid Earth (1978–2012), v. 116(B12). doi: 10.1029/2011JB008433.

Xu, S., Freeman, S.P.H.T., Rood, D.H., Shanks, R.M., 2015, Decadal ^{10}Be, ^{26}Al and ^{36}Cl QA measurements on the SUERC accelerator mass spectrometer, Nuclear Instruments and Methods B: Beam Interactions with Materials and Atoms, doi:10.1016/j.nimb.2015.03.064.

York, D., 1966, Least-squares fitting of a straight line: Canadian Journal of Physics, v. 44, no. 5, p. 1079-1086. doi: 10.1139/p66-090.

Tables:

Table 1. Sample location data

Site	Latitude*	Longitude*	Elevation (m)*	Sample interval (m)**	Sample height above strath (m)	Strath height (m)***
Potato Hill	46.9122	-120.4954	437	2.7-3.1	0.0-0.3	17 ± 2
Toth Road	46.9094	-120.4975	465	2.1-2.3	~2-3	56 ± 2
Mathews	46.8999	-120.4937	427	4.7-4.9	~1	20 ± 1
Meander	46.8539	-120.4649	400	6.6-6.8	0.2-0.4	11 ± 1
Higher Island	46.8342	-120.4589	474	1.7-1.9	0.0-0.2	95 ± 3
Lower Island	46.8339	-120.4563	441	2.0-2.3	~1	58 ± 2
Death Chute	46.8090	-120.4411	405	4.3-4.6	0.7-1.0	30 ± 1
Big Pines	46.8015	-120.4618	365	5.3-5.6	~2	3 ± 1

*UTM coordinates
**from 2008 GeoEarthscope lidar dataset, references the ellipsoid vertical datum
***sample interval measured from top of exposure or pit
****equal to mean of strath elevations minus corresponding Yakima River water surface elevation. Uncertainties represent 1 standard deviation about the mean height.

Table 2. Site deposit ages

Site name	Site ID*	^{26}Al-^{10}Be ages (Ma)**	IRSL ages (ka)***
Potato Hill	YK-01	2.94 ± 0.10	--
Toth Road	YK-05	1.13 ± 0.20	--
Rattlesnake Dance	YKX-02	0.30 ± 0.10	84.2-93.3
Lower Island	YKX-06	1.60 ± 0.10	--
Death Chute	YKX-03	0.90 ± 0.10	--
Big Pines	YK-03	0.00 ± 0.20	--
Meander	YK-04	1.60 ± 0.10	--

*YK- denotes site initially sampled by Coppersmith et al. (2014), and re-sampled in this study. YKX- denotes site first mapped and sampled in this study.
**This study, burial ages of gravel deposits.
***Ladinsky (2012), age of loess over gravel (therefore minimum limit for terrace age)
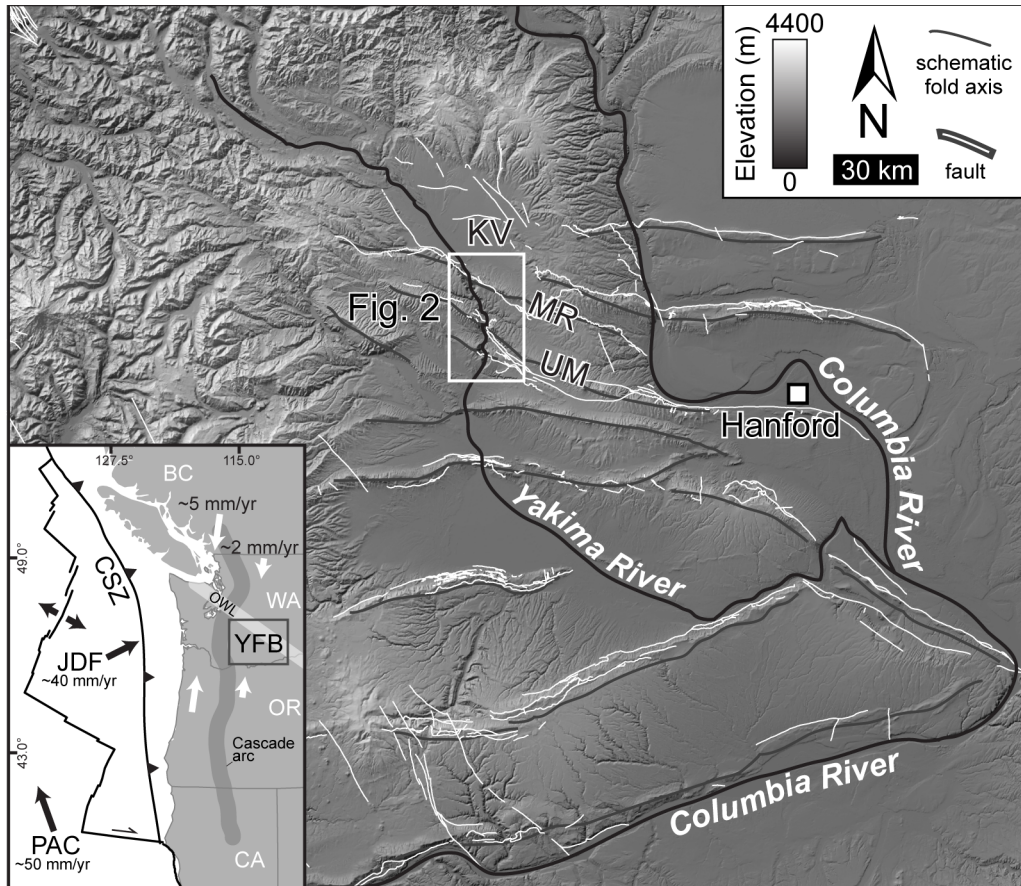
Figure 1. Structural and topographic map of the Yakima fold and thrust belt in central Washington. Map depicts study area in the Yakima River Canyon across Manastash (MR) and Umtanum Ridge (UR) structures south of Kittitas Valley (KV) and west of the Hanford Nuclear Reservation. Grey lines represent known or suspected Quaternary-active faults from Washington Department of Natural Resources (WA DNR) (http://www.dnr.wa.gov/ResearchScience/Topics/GeosciencesData/Pages/gis_data.aspx). Inset shows the relationship between the Pacific plate (PAC), Juan de Fuca plate (JDF), Cascadia subduction zone (CSZ), Yakima fold belt (YFB) structures (e.g., Wells et al., 1998), and the Olympic-Wallowa Lineament (OWL) (Raisz, 1945). Inset also depicts contemporary NNE shortening across the Cascade forearc and backarc regions implied by geodesy (McCaffrey et al., 2013). Base hillshade and topographic maps derived from Washington 10 m DEM (http://gis.ess.washington.edu/data/raster/tenmeter/byquad/).

Figure 2. *Caption on page 36*

^{26}Al (atoms/g)

^{10}Be (atoms/g)

A. Potato Hill, Thorp gravel *(YK-01)*
t_b= 2.9 ± 0.1 Ma
slope = 1.67 ± 0.9
R^2= 0.98

B. Toth Road *(YK-05)*
t_b= 1.1 ± 0.1 Ma
slope = 4.15 ± 0.44
R^2= 0.95

C. Rattlesnake Dance *(YKX-02)*
t_b= 0.3 ± 0.1 Ma
slope = 5.83 ± 0.45
R^2= 0.91

D. Meander *(YK-04)*
t_b= 1.6 ± 0.1 Ma
slope = 3.27 ± 0.34
R^2= 0.89

E. Higher Island *(YKX-05)*
NO BURIAL AGE
slope = 6.96 ± 1.14
R^2= 0.67

F. Lower Island *(YKX-06)*
t_b= 1.6 ± 0.1 Ma
slope = 3.21 ± 0.40
R^2= 0.98

G. Death chute *(YKX-03)*
t_b= 0.9 ± 0.2 Ma
slope = 4.30 ± 0.43
R^2= 0.84

H. Big Pines *(YK-03)*
t_b= 0.0 - 0.2 Ma
slope = 6.75 ± 0.13
R^2= 0.85

Sample isotope concentrations
— Analyzed in regression
— Not analyzed in regression

Calculated model likelihood
high
low

Figure 3. *Caption on page 36*

Figure 2. Quaternary geologic map of the Yakima River Canyon, depicting strath terrace gravels and cosmogenic sample sites. Lettered boxes in (A) correspond to detail maps (B), (C), and (D). Lines of section in detail maps correspond to Figure 5 interpretive cross sections. Geologic mapping overlies 2008 GeoEarthScope lidar data (accessed through www.opentopography.org). Geologic and structural mapping in area of (B) is modified from (Ladinsky, 2012). Swath topography box indicates area profiled in Figures 6a and 7a. Source for base hillshade and structural data same as Figure 1.

Figure 3. Cosmogenic ^{26}Al-^{10}Be isochron plots for samples collected at each site, constructed using a Bayesian linear regression algorithm modeling the likelihood of 100,000 lines fit to the isotope data. Thin red crosses represent outliers omitted from isochron analysis. See text for discussion.
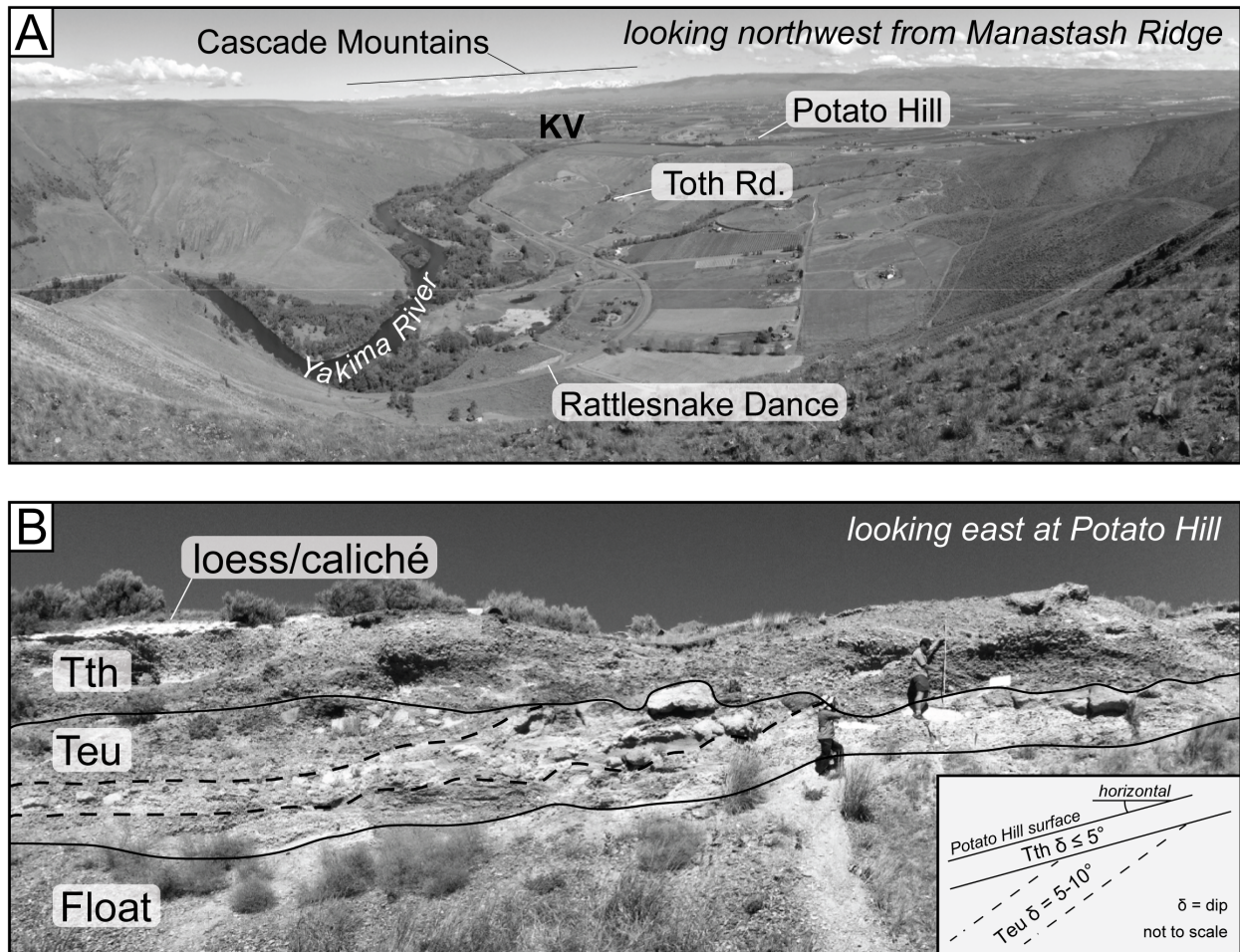
Figure 4. (A) View northwest from Manastash Ridge over Kittitas Valley (KV) and Manastash Ridge sample sites. (B) Potato Hill sample site depicting stratigraphic relationships observed in the field and described by Bentley (1977). Inset shows a simplified interpretation of the stratigraphy identified in the photo. Dashed lines represent internal bedding, possibly growth strata, in the Tertiary Upper Ellensburg (Teu) formation. The suspected growth strata dip 5-10° north and are truncated and capped by 2-3 m-thick ~2.9 Ma Thorp Gravel dipping up to 5° north. The Potato Hill surface dips in agreement with the Thorp Gravel (Tth), and is variably capped by thick caliche under loess. The white signboard marks the cosmogenic sample location, and the stadia rod is 2 m tall.
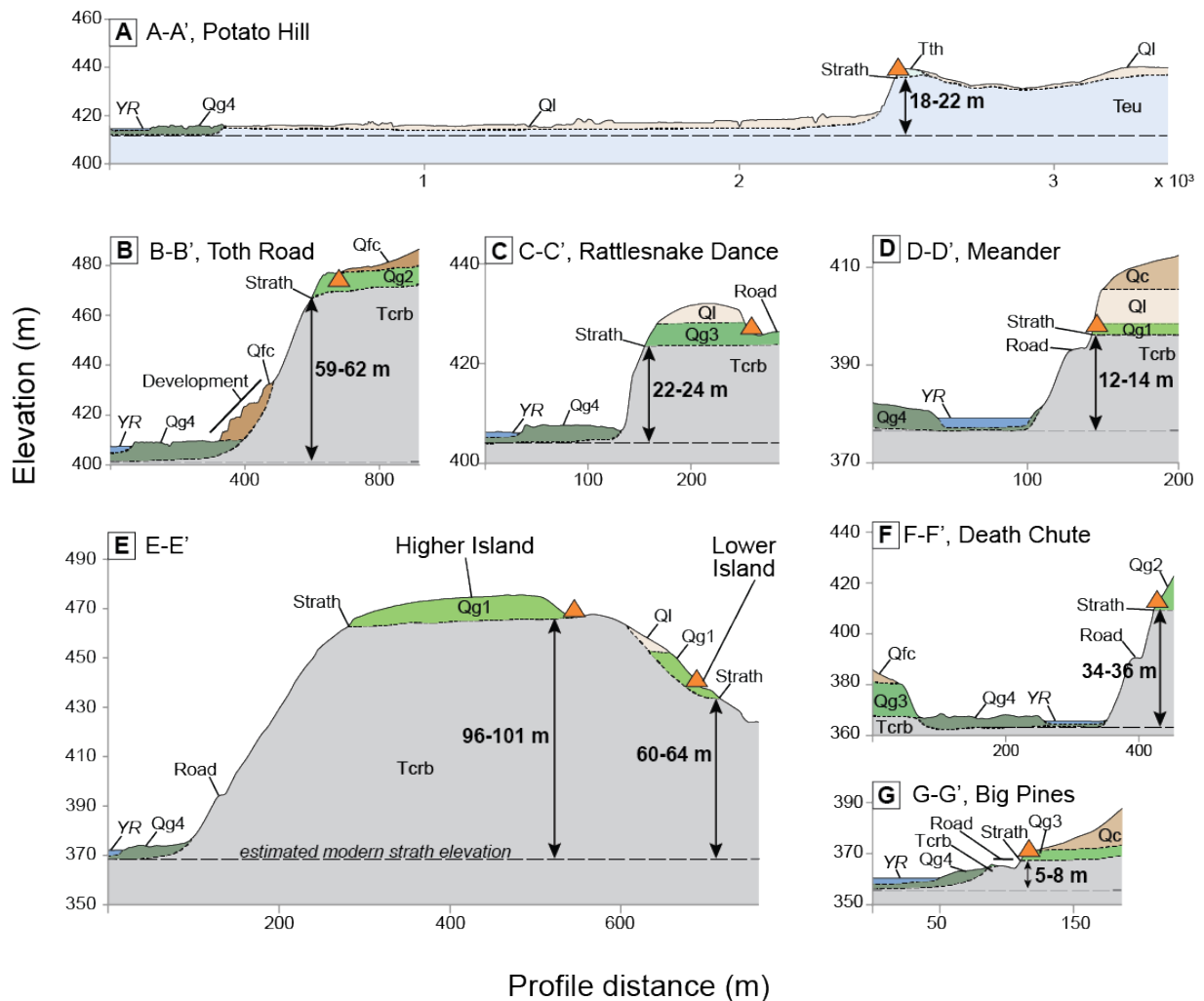
Figure 5. Interpretive cross sections through strath terrace sites sampled for ^{26}Al-^{10}Be isochron burial dating, based on geologic mapping in Figure 2. Symbology and geologic units explained in Figure 2. Profiles are shown by lettered lines in Figures 2B, 2C, and 2D, and topographic data are from 2008 GeoEarthScope lidar. Arrows indicate estimated Yakima River (YR) incision into the basalt strath at each sample site.
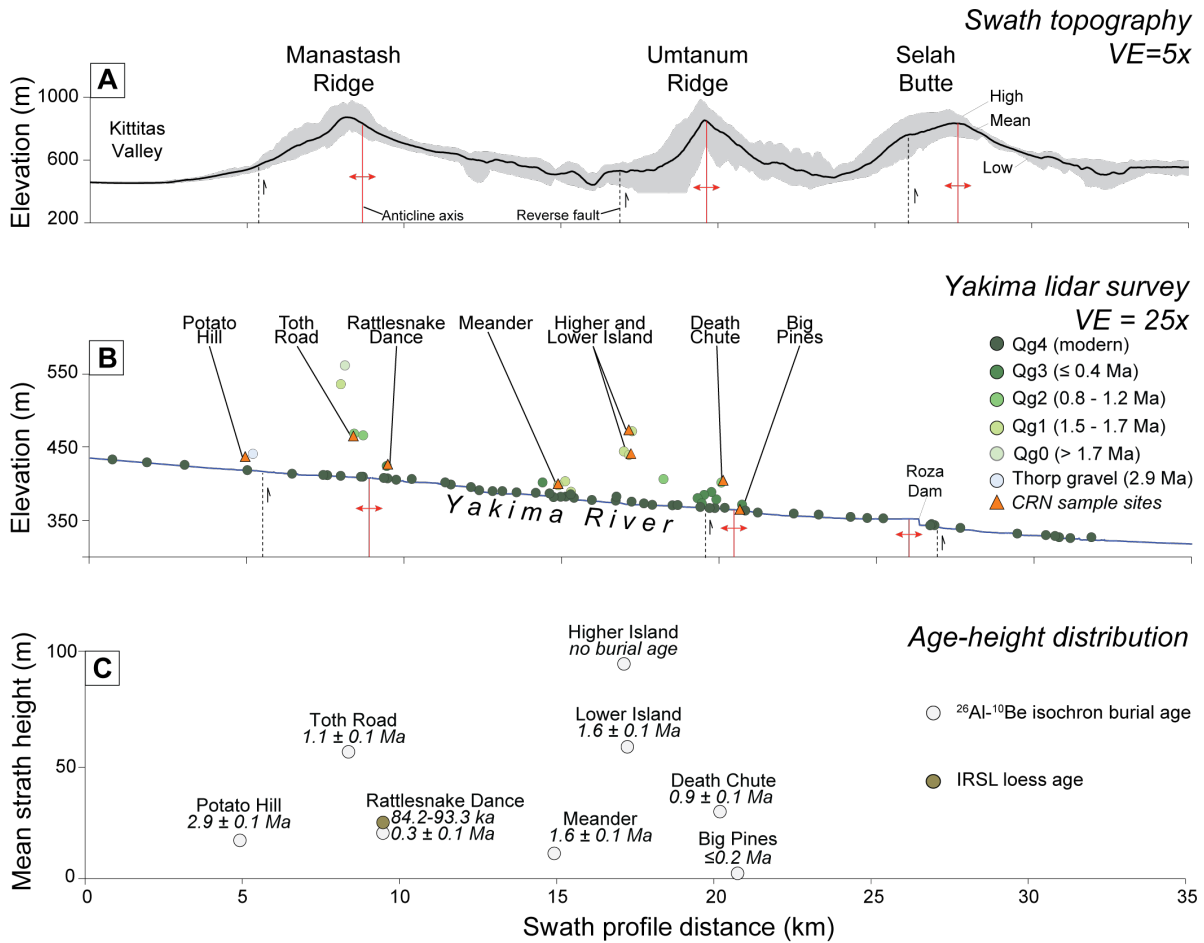
Figure 6. Profiles projected to the swath topography profile line (location shown in Figure 2A) comparing topography, structure, mapping results and cosmogenic burial age distribution. (A) 2.5 km-wide swath topographic profile (Figure 2A) from the 10 m DEM. The thick black profile line represents mean elevation and the grey envelope represents maximum and minimum elevations along the swath on Figure 2A. Structures are projected to line at approximate surface location, and represent the primary faults and folds associated with each ridge. (B) Cosmogenic sample sites, mean elevations of mapped strath terrace gravels, Yakima River long profile, and WA DNR structures projected below the river-surface intersection. (C) Cosmogenic ^{26}Al-^{10}Be isochron burial ages for each site plotted by height above the river (mean strath elevation minus river elevation) over profile distance.
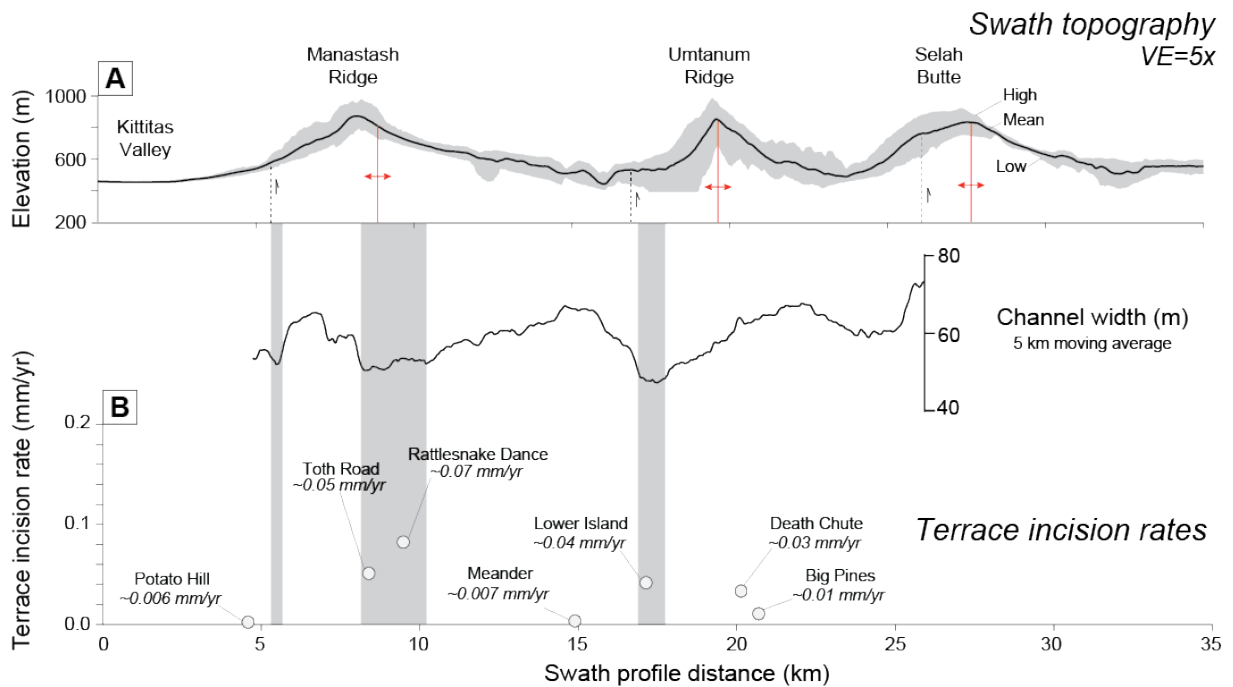
Figure 7. Profiles projected to the swath topography profile line (location shown in Figure 2A) comparing topography, structure, channel width, and incision rates. (A) Same as Figure 6A (B) Channel width (Fisher et al., 2013) and incision rates derived from cosmogenic ^{26}Al-^{10}Be isochron burial ages normalized to strath incision (this study). Grey bars show the interpreted correlation between narrow channel reaches, structures, and calculated incision rates.
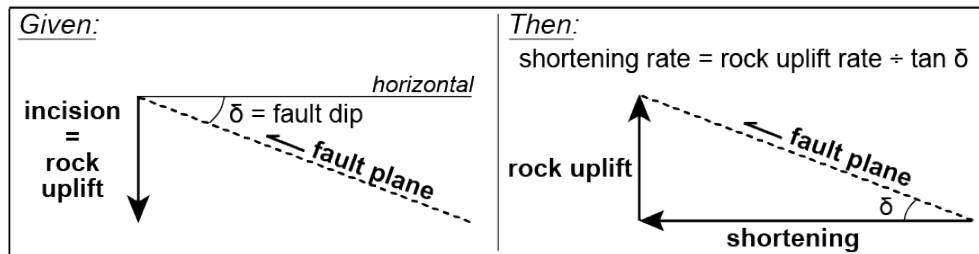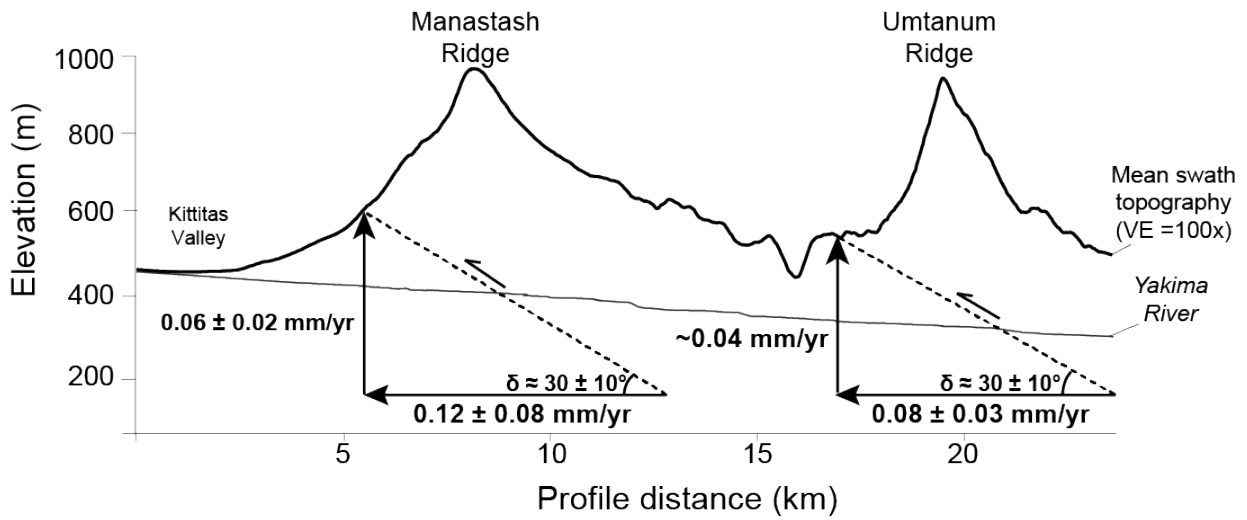
Figure 8. Simple 2d model estimating time-averaged shortening rates across south-dipping master reverse faults beneath Manastash and Umtanum Ridges. We equate rock uplift to the average bedrock incision rates across each fold. Topographic profile uses the same data as Figures 6A and 7A, and Yakima River profile is the same as in Figure 6B.

Appendix A: Sample processing

All samples were prepared for accelerator mass spectrometer analysis at the University of Vermont (UVM) Cosmogenic Isotope Laboratory facilities, following protocols described by Corbett et al. (2011). We washed, jaw-crushed, disc-milled, and sieved cobble and pebble samples to retain the medium to coarse sand (250-850 mm) fraction. We also sieved sand samples to retain the medium to coarse fraction, and separated magnetic grains from all samples. We subdivided non-magnetic 250-850 mm samples by modal estimation of quartz content, archiving samples with relatively low quartz content and purifying higher quartz content samples by a variation of the Kohl and Nishiizumi (1992) method.

Purification of higher quartz content samples consisted of successive acid etches varying in duration and acid strength, conducted in heated ultrasonic basins with intervening deionized water rinses. We etched samples twice (24 hours each) in 6N HCl to dissolve $CaCO_3$, Fe- and Al-oxide and hydroxide coatings, and remove adhered atmospheric ^{10}Be. We then etched each sample three times (24 hours each) in a 0.5% HF/HNO_3 mixture to dissolve most minerals except quartz, and dried, rinsed and visually inspected for dark (mafic) mineral grains. Where required, we removed mafic mineral grains from quartz by Lithium polytungstate density separation. We etched each sample in a 0.25% HF/ HNO_3 mixture, first for 72 hours, then again for one week before testing the purity of the resulting quartz separate.

We tested the purity of the isolated quartz by analyzing solutions of each sample on a JY Horiba inductively coupled plasma optical emission mass spectrometer (ICP-OES) to determine major element composition. We made solutions for ICP-OES major element analysis by dissolving ~250 mg of each sample in a mixture of concentrated HF and 0.5% H_2SO_4, evaporating, and bringing up the remaining bead of H_2SO_4 in 18 mega-ohm water. We etched the purified quartz a final time in the UVM cosmogenic clean laboratory for 8 hours in a mixture of 0.5% HF/HNO_3 and 18 mega-ohm water. We selected 30 quartz samples for Al and Be extraction based on purity and mass, and extracted the cosmogenic isotopes ^{26}Al and ^{10}Be in the UVM cosmogenic clean laboratory by column chromatography.

We prepared purified quartz aliquots for column chromatography in batches of 12, consisting of 10 samples and two process blanks. We massed and spiked each quartz sample with Al carrier sufficient to provide ~3000 mg per sample for analysis, and ~250 mg Be. Process blanks contained only Al and Be carrier, but we treated them like the other samples. We dissolved each sample in concentrated HF, split this solution, and spiked twos split from each sample with an internal standard containing Ga and Y, to make aliquots for determining total Al content by ICP-OES. We dried down the remaining solution with 2 ml $HClO_4$ four times to remove fluorides, leaving the sample as a cake, which we then dried down twice with 2 ml HCl to convert perchlorates to chlorides. We brought the chloride cakes back up in HCl, centrifuged the HCl solution to remove Ti oxides and other insoluble material, and passed the solution through anion resin columns to remove Fe.

After anion chromatography, we dried down each sample with H_2SO_4 and H_2O_2, brought each sample back up in 18 mega-ohm water, and passed each sample through cation resin columns to remove Ti, and isolate Al and Be. We evaporated the column acids from the Al and Be fractions, re-dissolved the samples in weak HNO_3, and took a small (respectively, 200 ml and 50 ml for Al and Be) aliquot to test yield purity of the resulting Al and Be separates by ICP-OES analysis. We added NH_4OH to each sample sufficient to precipitate Al and Be as hydroxides, washed the resulting hydroxide jells with 18 mega-ohm water, dried the jells slowly over low heat to produce pellets which we transferred into quartz crucibles, and oxidized over a natural gas flame in a fume hood.

We mixed and homogenized the resulting oxide powders with Ag and Nb (respectively for Al and Be) at a 1:1 molar ratio, packed each into a copper cathode, and shipped the cathodes to the SUERC accelerator mass spectrometer (AMS) facility in East Kilbride, Scotland for AMS

analysis of ^{26}Al and ^{10}Be (Xu et al., 2015). We normalized AMS measurements of ^{26}Al and ^{10}Be respectively to standards Z92-0222 (nominal ^{26}Al/^{27}Al ratio = 4.11 x 10^{-11}; Nishiizumi, 2004), and NIST (nominal ^{10}Be/^{9}Be ratio = 2.71 x 10^{-11}; Nishiizumi et al., 2007). We subtracted the isotopic ratios measured in the process blanks from the measured ratio of each sample as a blank correction, and calculated cosmogenic nuclide concentrations and related errors (atoms/g) by normalizing these blank-corrected values to sample quartz mass. We used the cosmogenic isochron burial method (Figure S1a-c) to determine burial ages from these concentrations.

Appendix B: Deposit descriptions
   In the field we characterized each Quaternary strath terrace gravel by measuring deposit thickness and counting gravel clasts for rock type (basalt, Cascade volcanic, non-volcanic).
   The Thorp gravel at Potato Hill is moderately cemented and consists of very poorly sorted, matrix supported, predominately well-rounded, sand to large cobble sized clasts Clasts (n = 50) in the Thorp gravel at Potato Hill are predominately basalt (60%), and Cascade volcanic (18%) (Figure S3).
   The Toth Road gravel (Figure S4a-b) consists of very poorly sorted, matrix supported, predominately well-rounded, sand to large cobble sized clasts. Gravel clasts (n = 50) are predominately basalt (34%), and Cascade volcanic (34%).
   The Mathews Terrace gravel (Figure S5a-b) is very poorly sorted, clast supported, and contains mostly well rounded, sand to medium cobble sized clasts. Gravel clasts (n = 50) are predominately basalt (58%), and Cascade volcanic (22%).
   The Meander Terrace gravel (Figure S6a-b) is very poorly sorted, clast-supported, and contains mostly well-rounded, sand to large cobble sized clasts, with common cross-bedded coarse sand lenses. Gravel clasts (n = 50) in the Meander Terrace gravel are predominately basalt (58%), and non-volcanic (28%).
   The Lower and Higher Island terrace gravels (Figures S7a-c) are very poorly sorted, clast supported, and contains mostly well rounded, sand to small boulder sized clasts. Gravel clasts (n = 52) in the Lower Island terrace gravel (Figures S8a-b, 9a-b) are predominately Cascade volcanic (29%), and non-volcanic (52%). Gravel clasts (n = 48) in the Higher Island gravel (Figures S10a-b) are predominately basalt (35%), and non-volcanic (44%).
   The Death Chute terrace (Figure S11a-b) gravel is very poorly sorted, clast supported, and contains mostly well rounded, sand to small boulder sized clasts. Gravel clasts (n = 45) are predominately Cascade volcanic (27%), and non-volcanic (53%).
   The Big Pines terrace (Figure S12a-b) gravel is very poorly sorted, clast-supported, and contains mostly well-rounded, sand to large cobble sized clasts. Big Pines gravel clasts (n = 50) are predominately basalt (64%), and Cascade volcanic (20%).

Appendix references:

Corbett, L. B., Young, N. E., Bierman, P. R., Briner, J. P., Neumann, T. A., Rood, D. H., and Graly, J. A., 2011, Paired bedrock and boulder 10 Be concentrations resulting from early Holocene ice retreat near Jakobshavn Isfjord, western Greenland. Quaternary Science Reviews, v. 30, no. 13, p. 1739-1749. doi:10.1016/j.quascirev.2011.04.001

Granger, D. E., & Smith, A. L., 2000, Dating buried sediments using radioactive decay and muogenic production of 26 Al and 10 Be. Nuclear instruments and methods in physics research section B: beam interactions with materials and atoms, v. 172, no. 1, p. 822-826. http://dx.doi.org/10.1016/S0168-583X(00)00087-2

Kohl, C. P., and Nishiizumi, K., 1992, Chemical isolation of quartz for measurement of in-situ-produced cosmogenic nuclides. Geochimica et Cosmochimica Acta, v. 56, no. 9, p. 3583-3587. http://dx.doi.org/10.1016/0016-7037(92)90401-4

Nishiizumi, K., 2004, Preparation of 26 Al AMS standards: Nuclear Instruments and Methods in Physics Research Section B: Beam Interactions with Materials and Atoms, v. 223, p. 388-392. doi: 10.1016/j.nimb.2004.04.075.

Nishiizumi, K., Imamura, M., Caffee, M. W., Southon, J. R., Finkel, R. C., & McAninch, J., 2007, Absolute calibration of 10 Be AMS standards. Nuclear Instruments and Methods in Physics Research Section B: Beam Interactions with Materials and Atoms, v. 258, no. 2, p. 403-413. doi:10.1016/j.nimb.2007.01.297.

Table S1. Cosmogenic isotope data

Site	Sample ID	UVM ID	SUERC Be #	SUERC Al #	Quartz (g)	9Be (ug)	27Al (ug)	Measured 10/9 Be ratio	± 1σ	Measured 26/27 Al ratio	± 1σ	***Blank corrected 10Be atoms/g	± 1σ	****Blank corrected 26Al atoms/g	± 1σ	26Al/10Be ratio	± 1σ
Potato Hill	YK-01A	V564A	b9266	a2394	12.29	257.48	3060	1.12E-13	4.59E-15	1.44E-13	6.47E-15	1.45E+05	6.62E+03	7.93E+05	3.60E+04	5.49	0.35
	YK-01D	V564B	b9267	a2395	23.85	256.53	2818	2.80E-13	7.67E-15	3.46E-13	1.05E-14	1.95E+05	5.57E+03	9.10E+05	2.77E+04	4.66	0.19
	YK-01E	V564C	b9270	a2396	19.86	256.63	3988	3.88E-13	9.46E-15	2.46E-13	1.03E-14	3.27E+05	8.22E+03	1.10E+06	4.60E+04	3.35	0.16
	YKX-01RF	V564L	b9280	a2408	39.94	255.90	4881	3.59E-13	8.34E-15	2.59E-13	9.12E-15	1.50E+05	3.60E+03	7.05E+05	2.49E+04	4.70	0.20
Toth Road	YK-05RC	V564D	b9271	a2397	39.06	257.27	1863	1.51E-13	4.47E-15	3.59E-13	1.09E-14	6.29E+04	2.03E+03	3.81E+05	1.16E+04	6.06	0.27
	YK05A*	V521I	b7103	a1808	18.07	249.88	2948	6.03E-14	2.80E-15	9.38E-14	5.30E-15	5.34E+04	2.60E+03	3.38E+05	1.93E+04	6.33	0.47
	YK05B*	V521J	b7104	a1809	19.43	248.03	2880	9.37E-14	3.90E-15	1.37E-13	7.00E-15	7.79E+04	3.20E+03	4.51E+05	2.32E+04	5.79	0.38
	YK05C*	V521K	b7105	a1810	21.11	247.99	2939	9.60E-14	3.30E-15	1.36E-13	6.10E-15	7.34E+04	2.60E+03	4.21E+05	1.90E+04	5.74	0.33
	YK05F*	V521L	b7107	a1812	20.22	251.70	2849	9.99E-14	3.70E-15	1.40E-13	6.60E-15	8.10E+04	3.10E+03	4.37E+05	2.07E+04	5.40	0.33
	YK-5RE	V568H	b9260	a2419	15.14	257.17	2830	5.15E-14	2.64E-15	1.05E-13	4.59E-15	5.47E+04	3.06E+03	4.36E+05	1.92E+04	7.97	0.57
Rattlesnake	YKX-02C	V564H	b9276	a2403	25.20	256.02	9521	1.72E-13	5.25E-15	9.24E-14	4.36E-15	1.11E+05	3.65E+03	7.72E+05	3.68E+04	6.97	0.40
	YKX-02E	V562A	b9235	a2378	37.56	256.60	5746	2.63E-13	6.68E-15	2.47E-13	1.11E-14	1.18E+05	3.19E+03	8.39E+05	3.77E+04	7.09	0.37
	YKX-02F	V564I	b9277	a2404	13.22	256.90	2741	8.03E-14	3.76E-15	1.68E-13	1.01E-14	9.34E+04	5.10E+03	7.75E+05	4.69E+04	8.31	0.68
	YKX-02G	V562B	b9237	a2380	39.97	254.92	4097	2.53E-13	6.80E-15	3.16E-13	1.01E-14	1.06E+05	3.03E+03	7.21E+05	2.31E+04	6.80	0.29
	YKX-02M	V564E	b9272	a2400	37.06	256.96	3594	2.23E-13	6.05E-15	3.31E-13	1.21E-14	9.93E+04	2.85E+03	7.14E+05	2.61E+04	7.19	0.33
	YKX-02O	V568G	b9259	a2417	12.08	245.97	2575	1.06E-13	5.63E-15	1.93E-13	1.01E-14	1.40E+05	7.70E+03	9.13E+05	4.79E+04	6.50	0.49
Meander	YK-04RF	V568I	b9261	a2420	20.17	256.08	4979	3.54E-14	2.56E-15	2.83E-14	1.98E-15	2.72E+04	2.22E+03	1.51E+05	1.09E+04	5.55	0.61
	YK04A*	V521E	b7096	a1802	21.81	249.10	2957	4.99E-14	2.40E-15	6.42E-14	3.8E-15	3.63E+04	1.80E+04	1.92E+05	1.13E+04	5.29	2.64
	YK04B*	V521F	b7097	a1803	20.97	248.81	3062	2.68E-14	1.70E-15	4.30E-14	2.9E-15	1.94E+04	1.30E+04	1.37E+05	9.40E+04	7.06	4.87
	YK04D*	V521G	b7101	a1806	22.41	248.21	6656	3.57E-14	2.20E-15	2.33E-14	2.2E-15	2.46E+04	1.60E+03	1.49E+05	1.45E+04	6.06	0.71
	YK04E*	V521H	b7102	a1807	22.40	248.60	2896	3.57E-14	1.50E-15	5.23E-14	4.0E-15	2.10E+04	1.10E+03	1.48E+05	1.14E+04	7.05	0.66
	YK-04S	V568J	b9263	a2421	13.90	258.00	4040	2.50E-14	1.76E-15	2.02E-14	1.58E-15	2.69E+04	2.30E+03	1.25E+05	1.03E+04	4.66	0.55
Higher Island	YKX-05H	V562F	b9241	a2384	30.60	256.87	3509	1.13E-13	4.81E-15	1.44E-13	5.65E-15	6.10E+04	2.93E+03	3.66E+05	1.45E+04	5.99	0.37
	YKX-05L	V562G	b9244	a2387	39.84	256.66	6010	1.64E-13	6.35E-15	1.34E-13	5.77E-15	6.90E+04	2.87E+03	4.48E+05	1.95E+04	6.49	0.39
	YKX-05N	V562I	b9246	a2389	25.57	256.63	2544	9.67E-14	4.77E-15	1.84E-13	6.39E-15	6.24E+04	3.48E+03	4.07E+05	1.42E+04	6.53	0.43
	YKX-05O	V562J	b9247	a2390	38.06	256.81	5060	1.43E-13	5.07E-15	1.32E-13	5.76E-15	6.29E+04	2.46E+03	3.89E+05	1.71E+04	6.19	0.36
	YKX-05P	V568E	b9257	a2415	17.15	257.20	3204	6.92E-14	3.13E-15	9.79E-14	4.62E-15	6.60E+04	3.19E+03	4.05E+05	1.93E+04	6.13	0.42
	YKX-05Q	V562K	b9248	a2391	26.12	256.11	3278	1.13E-13	5.80E-15	1.53E-13	5.80E-15	7.17E+04	3.04E+03	4.27E+05	1.63E+04	5.96	0.34
Lower Island	YKX-06H	V568B	b9252	a2410	40.02	257.33	3661	1.46E-13	5.14E-15	1.92E-13	7.03E-15	6.12E+04	2.22E+03	3.90E+05	1.44E+04	6.36	0.33
	YKX-06J	V568K	b9264	a2422	8.46	255.38	2467	4.10E-14	2.18E-15	6.92E-14	3.85E-15	7.60E+04	4.54E+03	4.45E+05	2.51E+04	5.86	0.48
	YKX-06K	V568C	b9253	a2413	20.27	256.05	2668	9.64E-14	3.72E-15	1.53E-13	5.83E-15	7.85E+04	3.18E+03	4.46E+05	1.71E+04	5.68	0.32
	YKX-06P	V568D	b9254	a2414	15.17	255.10	2925	5.62E-14	2.80E-15	8.11E-14	3.50E-15	5.95E+04	3.21E+03	3.45E+05	1.51E+04	5.80	0.40
	YKX-06R	V562L	b9250	a2393	26.85	255.35	3539	8.51E-14	3.62E-15	1.26E-13	5.47E-15	5.17E+04	2.64E+03	3.68E+05	1.61E+04	7.13	0.48
Death Chute	YKX-03C	V568F	b9258	a2416	11.39	272.57	2623	1.27E-14	1.54E-15	2.10E-14	1.63E-15	1.51E+04	2.62E+03	1.03E+05	8.44E+03	6.86	1.32
	YKX-03F	V564K	b9279	a2407	14.43	256.38	2566	2.10E-14	1.51E-15	2.93E-14	2.04E-15	1.50E+04	2.24E+03	1.13E+05	8.15E+03	7.55	1.25
	YKX-03K	V562D	b9239	a2382	34.76	256.81	4382	4.54E-14	2.88E-15	4.87E-14	2.65E-15	2.06E+04	1.74E+03	1.35E+05	7.48E+03	6.55	0.66
	YKX-03M	V562C	b9238	a2381	33.80	256.75	4359	3.80E-14	2.37E-15	3.39E-14	2.30E-15	1.74E+04	1.59E+03	9.50E+04	6.65E+03	5.46	0.63
	YKX-03O	V564J	b9278	a2406	33.18	257.17	5396	7.17E-14	2.99E-15	4.74E-14	2.59E-15	3.27E+04	1.66E+03	1.69E+05	9.43E+03	5.16	0.39
Big Pines	YK03B*	V521A	b7091	a1797	22.09	248.10	4809	4.88E-14	2.50E-15	4.48E-14	3.21E-15	3.48E+04	1.90E+03	2.14E+05	1.52E+04	6.15	0.55
	YK03E*	V521B	b7093	a1799	24.79	249.63	2996	6.95E-14	2.80E-15	1.30E-13	5.10E-15	4.51E+04	1.90E+03	3.47E+05	1.36E+04	7.69	0.44
	YK03C*	V521D	b7095	a1801	10.08	249.38	2820	1.86E-14	1.80E-15	3.10E-14	2.70E-15	2.67E+04	2.70E+03	1.88E+05	1.65E+04	7.04	0.94
**Blanks	V521*	V521C	b7094	a1800	0.00	248.95	2940	2.39E-15	6.60E-16	8.38E-16	4.20E-16						
	V562	V562E	b9240	a2383	0.00	256.7	2497	2.32E-15	8.19E-16	6.28E-16	4.44E-16						
	V568	V568A	b9251	a2409	0.00	257.6	2502	2.91E-15	8.77E-16	1.12E-15	5.58E-16						
	V564	V564F	b9273	a2401	0.00	257.3	2496	7.62E-15	9.53E-16	1.08E-15	7.67E-16						
	V562X	V562H	b9245	a2388	0.00	256.0	2502	5.20E-15	1.08E-15	9.82E-16	5.67E-16						
	V568X	V568L	b9265	a2423	0.00	256.5	2473	3.72E-15	9.02E-16	6.91E-16	3.99E-16						
	V564X	V564G	b9274	a2402	0.00	256.7	2493	9.22E-15	1.18E-15	7.54E-16	4.35E-16						

Samples measured at SUERC AMS.
*Sampled and measured by (Coppersmith et al., 2014)
**Batch specific blank used for correction, UVM ID indicates corresponding corrected batch #. Uncertainties (1σ) were propagated in quadrature.
***For 10Be, NIST standard was used with a nominal 10Be/9Be ratio of 2.71e-11.
****For 26Al, standard Z92 0222 was used for normalization with nominal 26Al/27Al ratio of 4.11e-11.
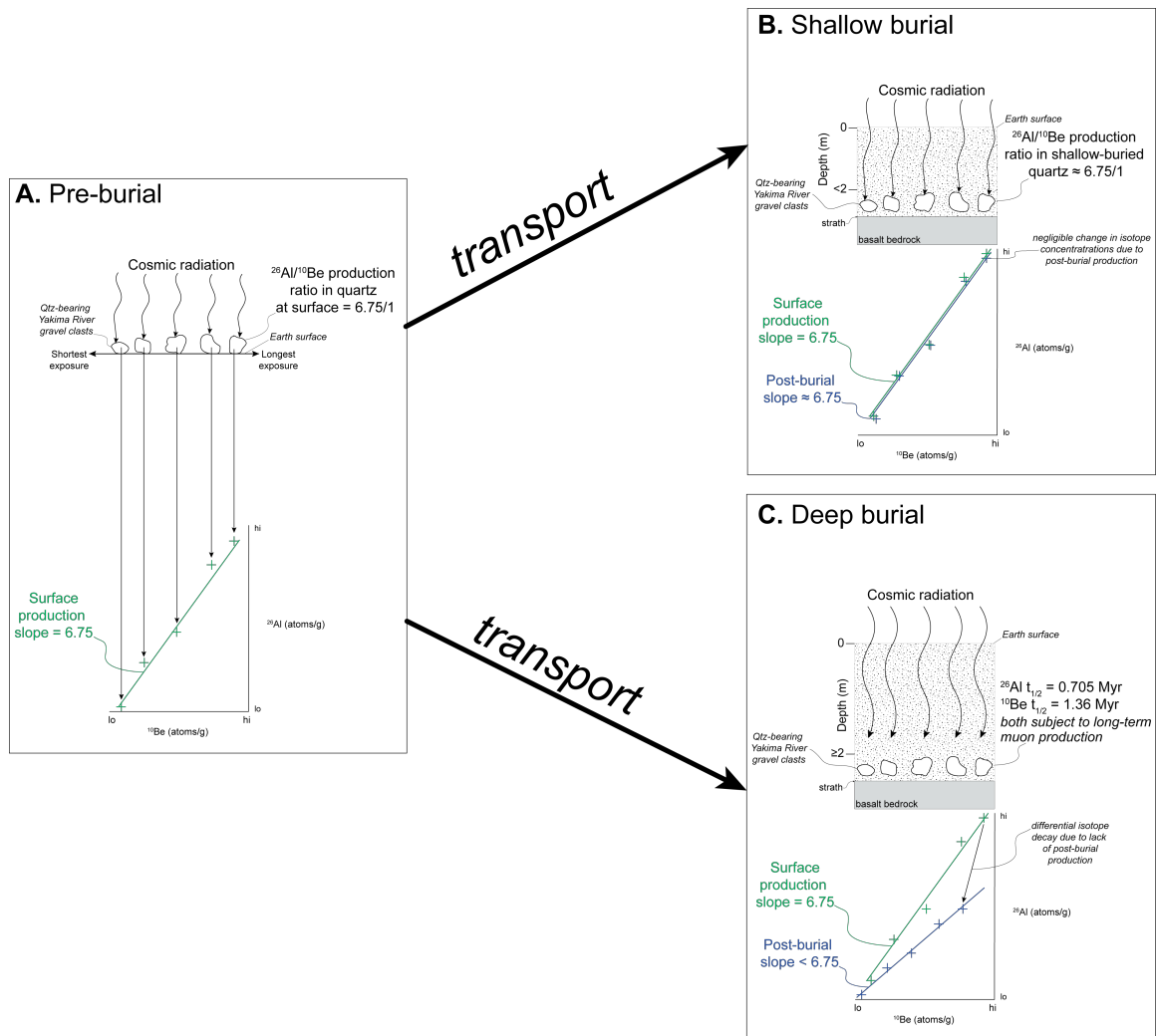
Figure S1. Conceptual diagram depicting the cosmogenic burial dating method applied to the Yakima River terrace gravels. (A) Accumulation of [26]Al and [10]Be in quartz within clasts at the surface of varying ages (for illustrative purposes the ages increase from left to right). The green crosses represent isotope concentrations, and the green best-fit line has a nominal slope of 6.75, reflecting the surface production ratio of [26]Al to [10]Be. (B) Clasts are transported and buried too shallow (<2 m) to shield from post-burial nuclide production (≥2 m) in a gravel deposit cut into a basalt strath. The post-burial production of cosmogenic [26]Al and [10]Be is such that the slope of a line (blue) fit to the measured post-burial isotope concentrations (blue crosses) roughly matches the surface production ratio. (C) Clasts are transported and buried sufficiently to shield from significant post burial nuclide inheritance (≥2 m) in a gravel deposit cut into a basalt strath. The subsequent decay of cosmogenic [26]Al and [10]Be at different rates drives the isotope concentrations down predictably such that the slope of a line (blue) fit to the measured post-burial isotope concentrations (blue crosses) reflects time-dependent deviation from the surface production ratio, and incorporates long term muonogenic production of [26]Al and [10]Be. For detailed discussion of muonogenic production of [26]Al and [10]Be in buried sediments, see (Granger and Smith, 2000).
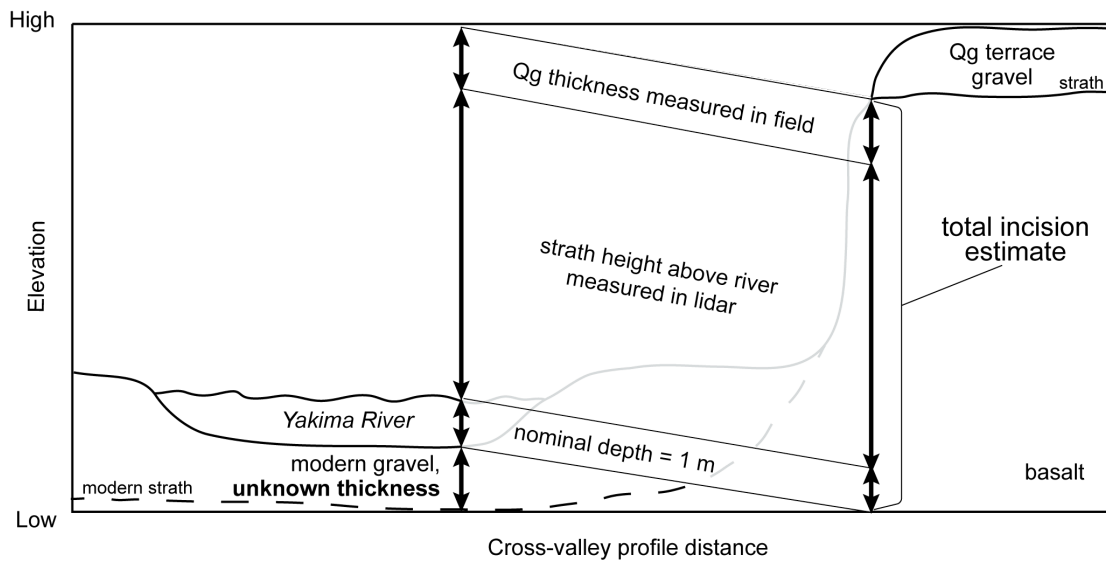
Figure S2. Schematic depiction of our approach to estimating total bedrock incision at each site (given unknown thickness of the modern gravel) as the sum of Quaternary terrace gravel (Qg) thickness, strath height, and a nominal 1 m Yakima River depth.

Figure S3. Potato Hill stratigraphy, field photo, and Thorp gravel rock type histogram. Orange triangle marks cosmogenic sample location.

Potato Hill

Light brown loess deposit with sandy soil developed in the upper 20-30 cm.

Bold white ~30 cm thick caliché.

Brown to reddish brown, very poorly sorted, moderately cemented matrix-supported gravel. Consists of coarse sand to coarse cobble sized, well rounded to subrounded mixed lithology clasts. Bottom 10-30 cm of unit is rusty brown and relatively well-cemented. Unit dips ~5° to the north, truncating bedding in the underlying unit. Thorp gravel after Bentley (1977). *strath*

Light grey to grey-brown, very poorly sorted, well-rounded to subrounded fine sand to medium boulder sized clasts, consist of almost entirely Cascade volcanics and boulder-sized tuffaceous blocks and lesser basaltic clasts. Generally matrix supported and weakly cemented. Unit has internal beds dipping 5-10° to the north. We follow Bentley (1977) in interpreting this unit as Tertiary Upper Ellensburg Formation.

f c | f c | f c | f c | f c
Sand | Gravel | Cobble | Boulder

Thorp gravel at Potato Hill
n = 50

A Toth

467

Elevation (m)

462

Sand Gravel Cobble Boulder

Light to medium brown, very poorlysorted matrix-supported gravel that consists of medium sand to fine boulder sized, well-rounded to subrounded mixed lithology clasts.

strath

Basalt

B Toth Road gravel
n = 50

# of clasts

40

20

0

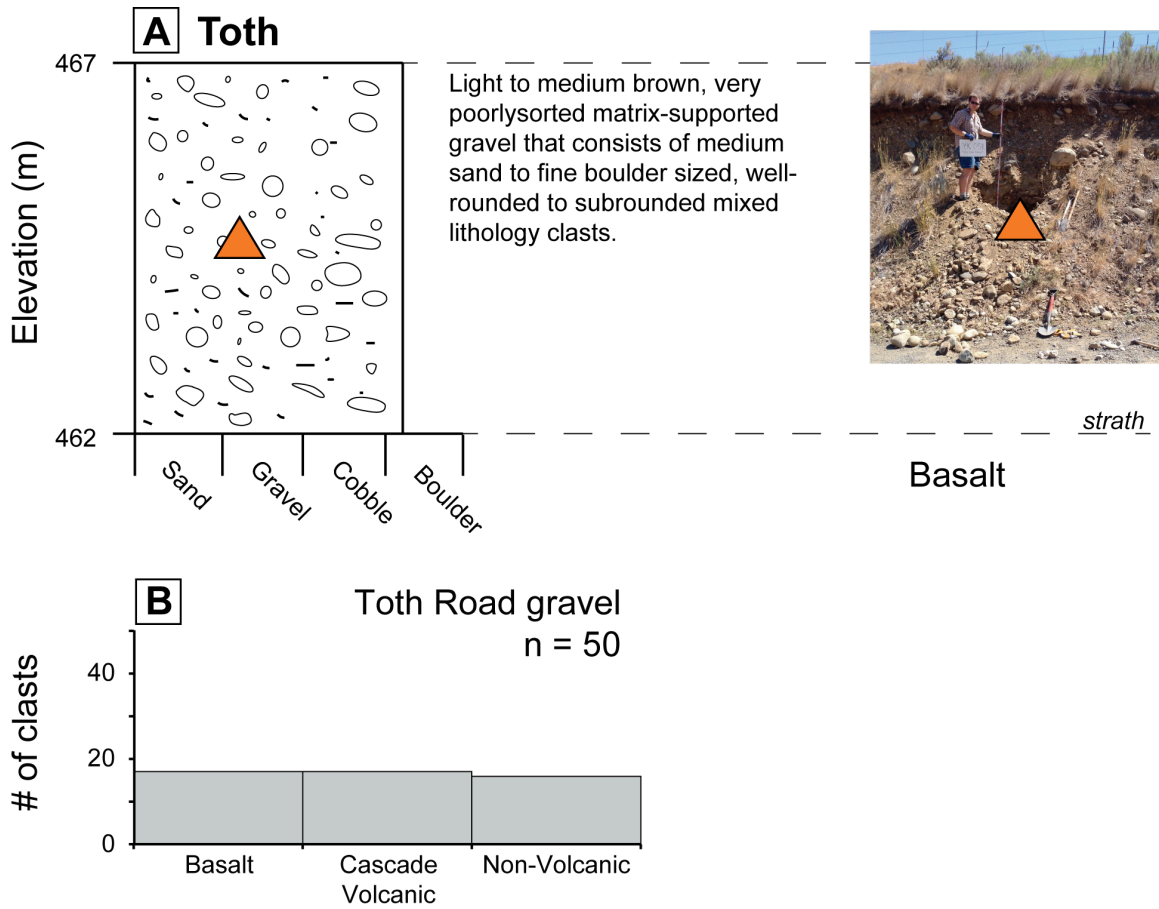Basalt   Cascade   Non-Volcanic
         Volcanic

Figure S4. (A) Toth Road gravel description and field photo. Orange triangle marks cosmogenic sample location. (B) Toth Road gravel rock type histogram.

A Rattlesnake Dance

Light brown massive loess deposit.

Light greyish brown, very poorly sorted clast-supported gravel deposit consisting of fine gravel to coarse cobble sized, well rounded to subangular mixed lithology clasts. Clasts commonly have well-developed (1-4 mm thick) caliché rinds.

strath

Basalt

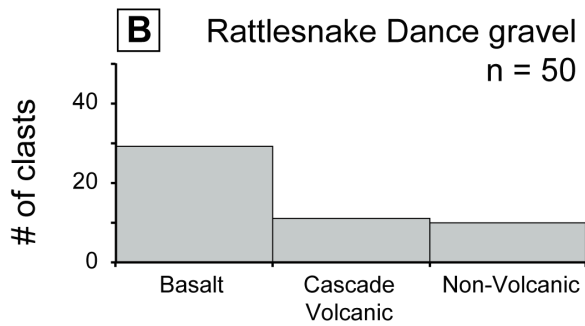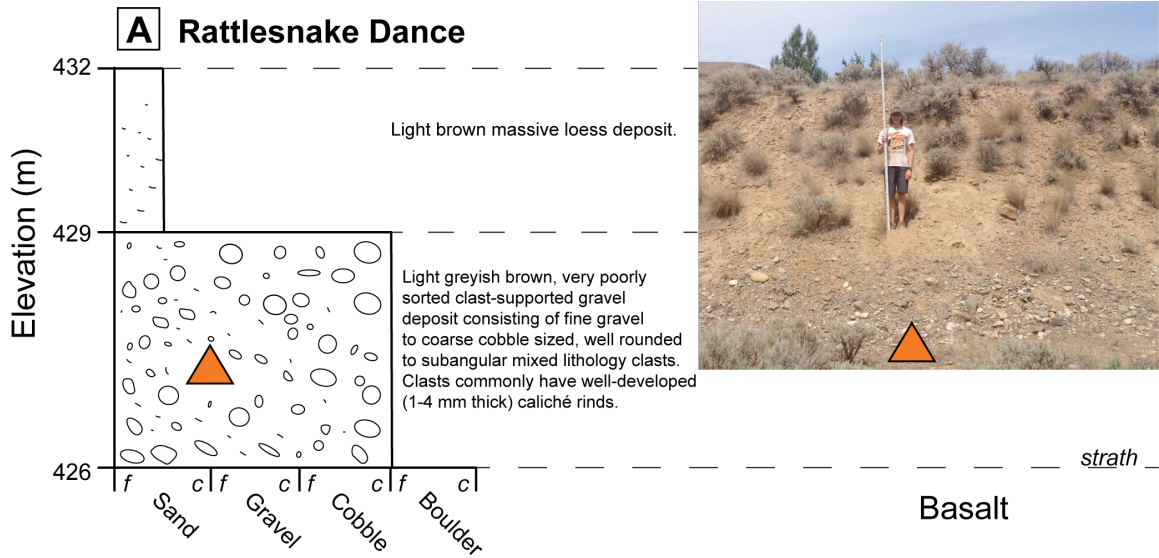**B** Rattlesnake Dance gravel

n = 50

Figure S5. (A) Rattlesnake Dance terrace stratigraphy and field photo. Orange triangle marks cosmogenic sample location. (B) Mathews terrace gravel rock type histogram.
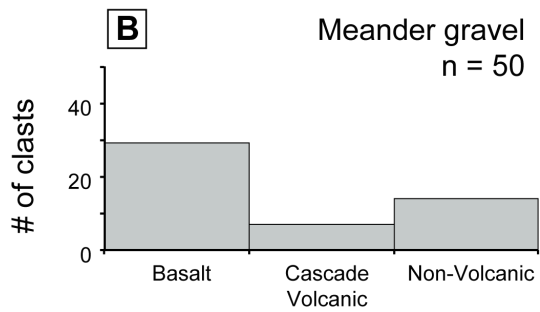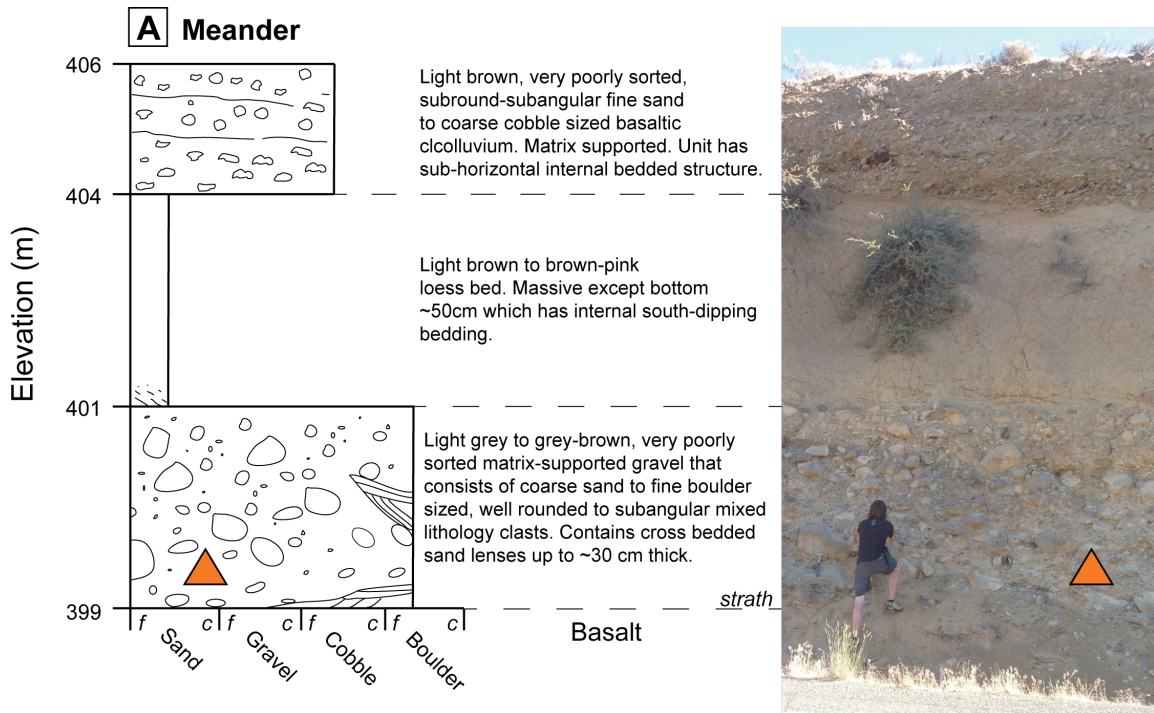
A Meander

Light brown, very poorly sorted, subround-subangular fine sand to coarse cobble sized basaltic clcolluvium. Matrix supported. Unit has sub-horizontal internal bedded structure.

Light brown to brown-pink loess bed. Massive except bottom ~50cm which has internal south-dipping bedding.

Light grey to grey-brown, very poorly sorted matrix-supported gravel that consists of coarse sand to fine boulder sized, well rounded to subangular mixed lithology clasts. Contains cross bedded sand lenses up to ~30 cm thick.

strath

Basalt

B Meander gravel
n = 50

Figure S6. (A) Meander terrace stratigraphy and field photo. Orange triangle marks cosmogenic sample location. (B) Toth Road gravel rock type histogram.
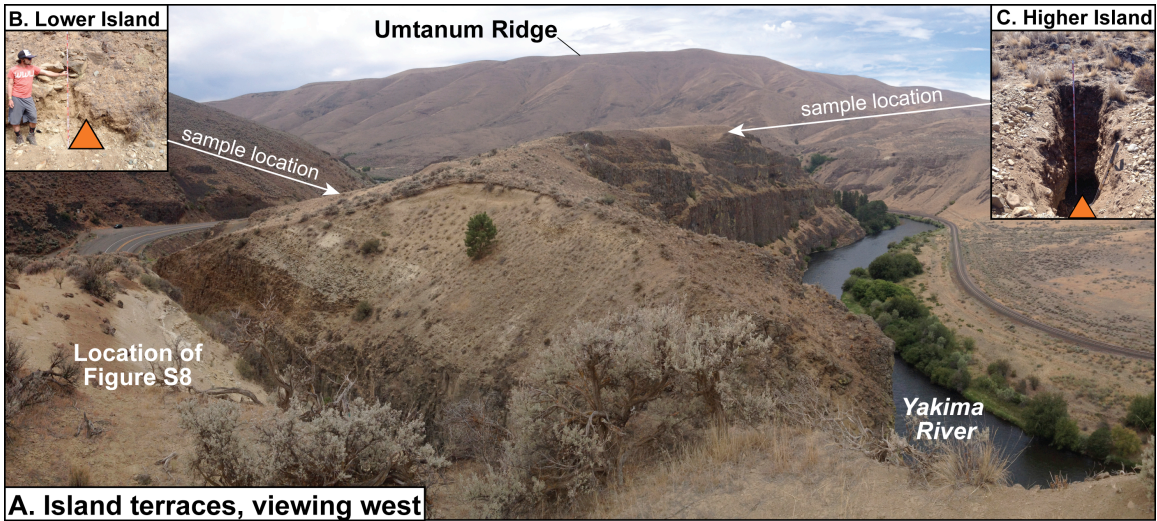
Figure S7. (A) Looking west at Island terrace sites. (B) Detail photo of Lower Island terrace sample site, location indicated on figure (A). (C) Detail photo of Higher Island terrace sample site, location indicated on figure (A). Orange triangles mark specific cosmogenic sample locations.
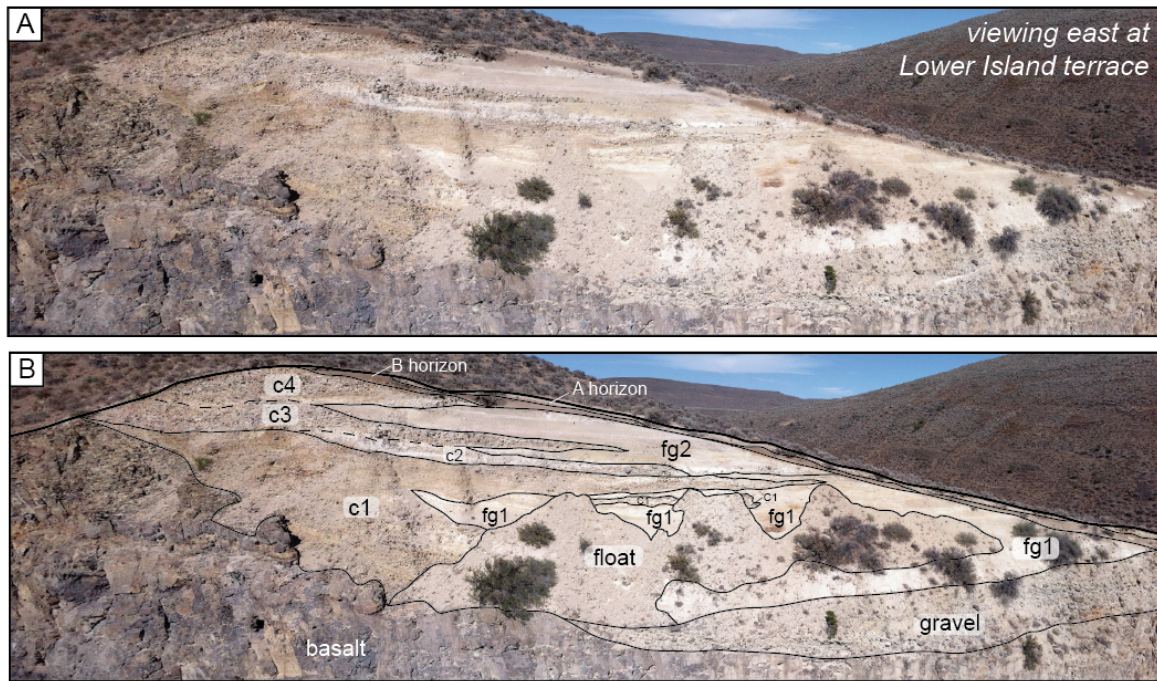

Figure S8. Lower Island terrace deposit photo (A) un-interpreted and (B) interpreted. Numbered units in (B) refer to interpreted depositional order (e.g., c1 deposited before c2, f1 deposited before f2, etc.) within the deposit, and correspond to descriptions in Figure S8 A.
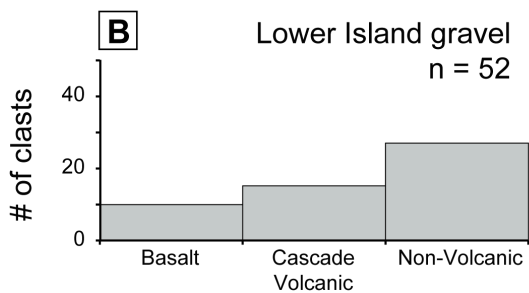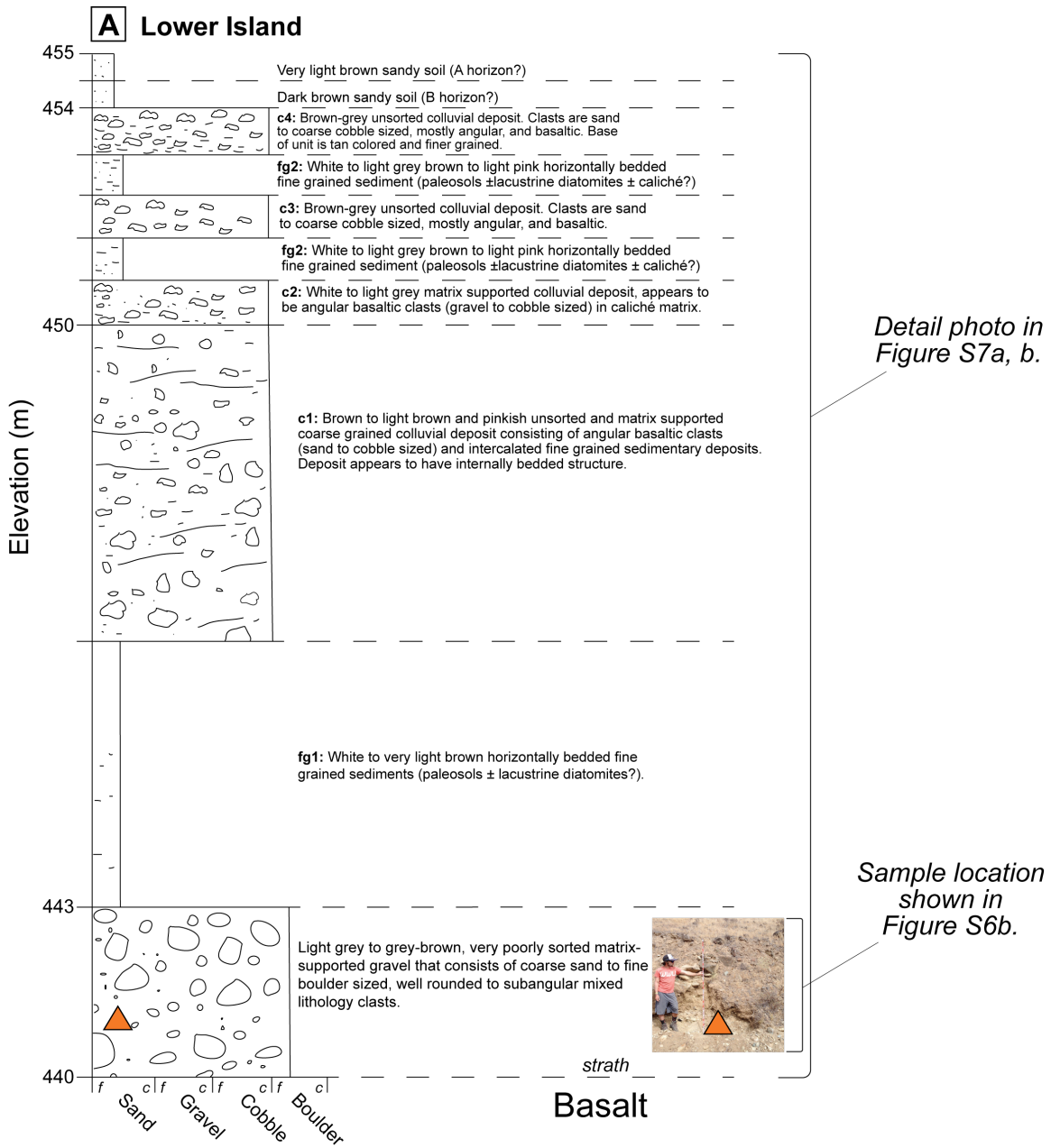
Figure S9. (A) Lower Island terrace stratigraphy and sample site photo. Orange triangles mark cosmogenic sample location. (B) Lower Island gravel rock type histogram.
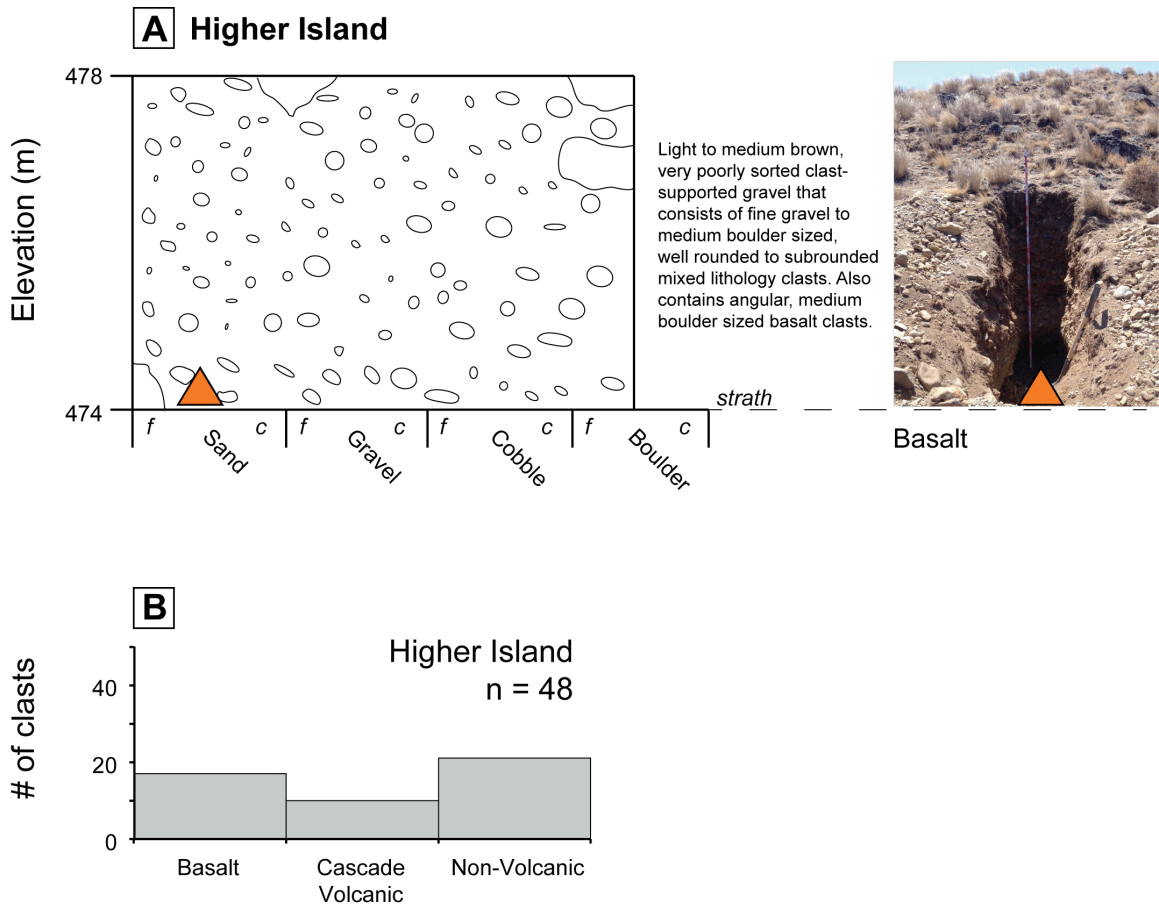
Figure S10. (A) Higher Island terrace deposit stratigraphy and sample location photo. Orange triangles mark cosmogenic sample location. (B) Higher Island gravel rock type histogram.

A Death Chute

Light brown to grey-brown, very poorly sorted, clast supported gravel consisting of mostly well round sand- to fine boulder-sized mixed lithology clasts.

strath
Basalt

Elevation (m)

410

405

f | c | f | c | f | c | f | c

Sand Gravel Cobble Boulder

B   Death Chute gravel
n = 45

# of clasts

40

20

0

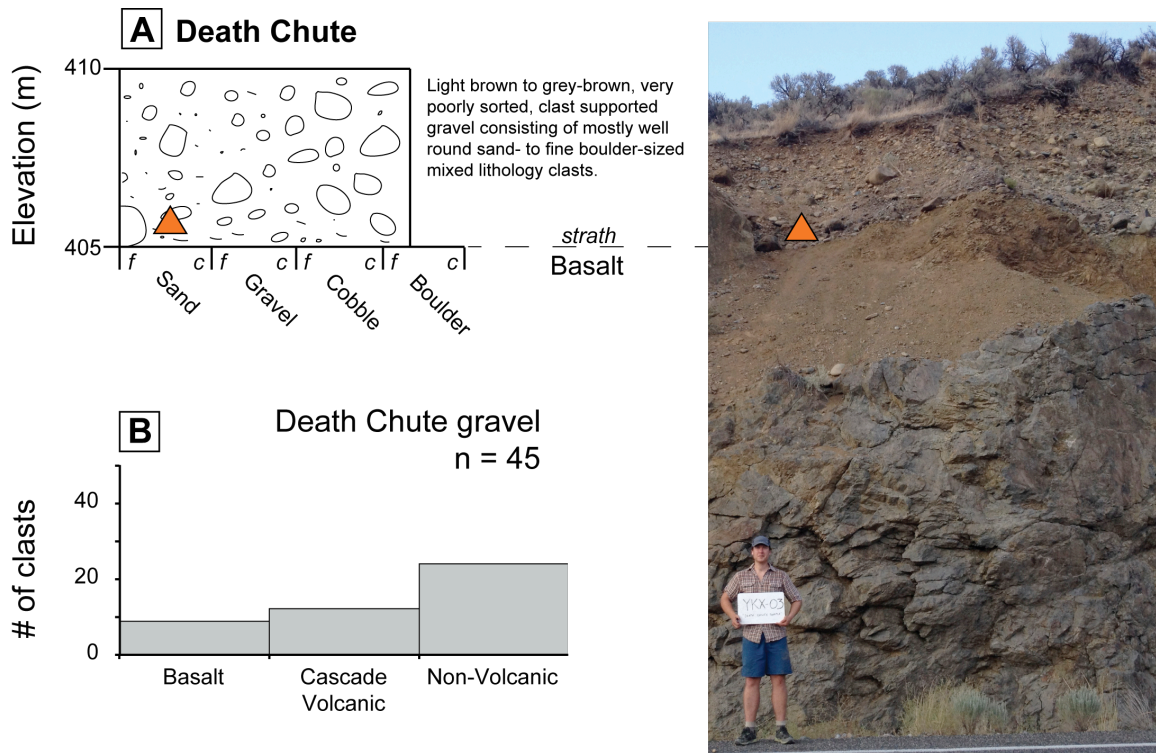Basalt | Cascade Volcanic | Non-Volcanic

Figure S11. (A) Death Chute terrace deposit stratigraphy and sample location photo. Orange triangles mark cosmogenic sample location. (B) Death Chute gravel rock type histogram.
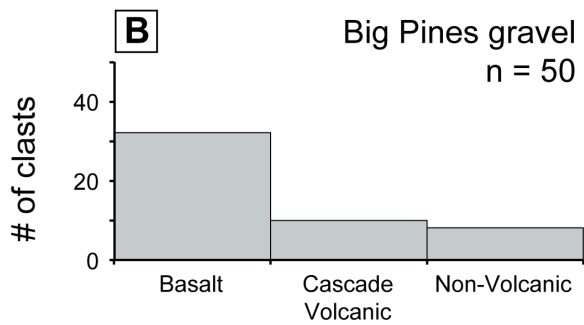
A Big Pines

Elevation (m)

369

365

Light brown to grey-brown, very poorly sorted, clast supported gravel consisting of mostly well rounded sand to fine boulder sized mixed lithology clasts. Unit contains massive 1-2 m thick beds that dip gently to the south. Top ~20 cm of gravel feature well-developed rocky brown soil.

strath

Basalt

f c f c f c f c

Sand Gravel Cobble Boulder

B Big Pines gravel
n = 50

# of clasts

40

20

0

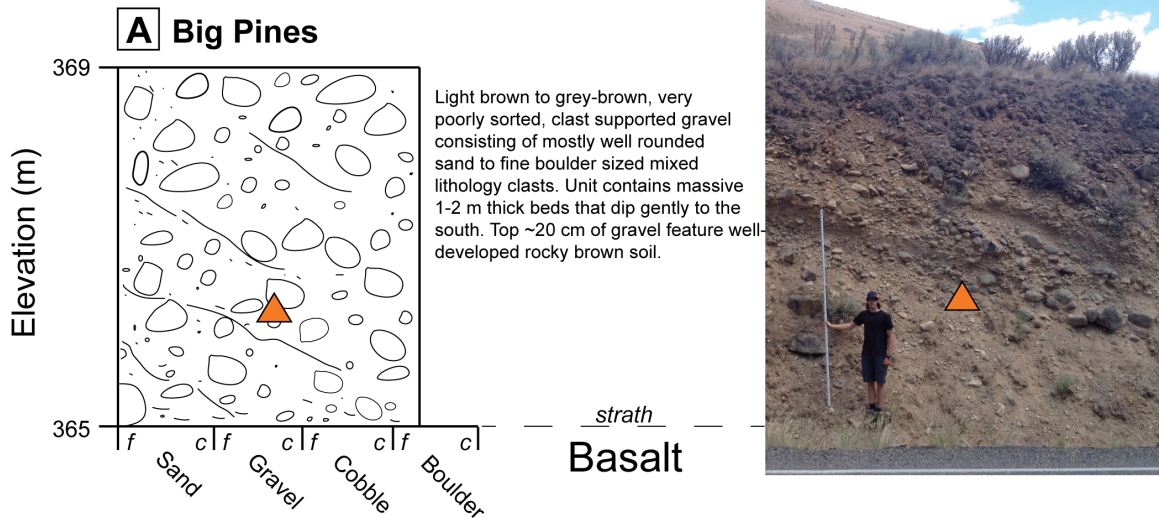Basalt   Cascade Volcanic   Non-Volcanic

Figure S12. (A) Big Pines terrace deposit stratigraphy and sample location photo. Orange triangles mark cosmogenic sample location. (B) Big Pines gravel rock type histogram.

Adrian M Bender   **Vita**
adrianmbender@gmail.com   15 June 2015

Education:
- BS, Geology; 2012; University of Alaska, Anchorage
- MS, Geology, 2015; Western Washington University

Geoscience work history:
- Core logging geologist, Kiska Metals; 2011
- Physical Scientist, US Geological Survey Alaska Science Center; 2012-present
- Graduate teaching assistant, Western Washington University; 2013-2014
- Graduate research assistant, Western Washington University; 2013-2015

Grants, awards and scholarships:
- Hecla-Greens Creek Scholarship: $3,400 (2011)
- Chugach Gem and Mineral Society Scholarship: $1,500 (2012)
- Fran Ulmer Transformative Research Award, UAA: $5,000 (2012)
- Global Change Research Grant, UA Statewide: $9,710 (2012)
- Geological Society of America Research Award: $1,500 (2014)
- Western Washington University Graduate Research Award: $800 (2014)

Publications:
Bender, A. M., Witter, R. C., & Rogers, M. (2015). Testing the use of bulk organic δ 13 C, δ 15 N, and C
      org: N tot ratios to estimate subsidence during the 1964 great Alaska earthquake. *Quaternary Science*
      Reviews, *113*, 134-146.
Bender, A. M., Amos, C. B., Bierman, P. R., Rood, D. H., Staisch, L. M., Kelsey, H. M., & Sherrod, B.,
      (submitted to *JGR Solid Earth*, June 2015). Differential Uplift and Incision of the Yakima River Terraces.

Meeting abstracts:
Bender, A. M., Witter, R. C., & Munk, L. A. (2012, December). Sediment geochemistry as potential sea-
      level indicators to assess coseismic vertical displacements above the Alaska-Aleutian megathrust. In *AGU*
      Fall Meeting Abstracts (Vol. 1, p. 1560).
Strupler, M., Moernaut, J., Haeussler, P. J., De Batist, M. A., & **Bender, A. M.** (2012, December). A
      reconnaissance survey of southern Alaskan lakes by high-resolution reflection seismics and short sediment
      coring-a first step towards a calibrated lacustrine paleoseismometer at the Alaskan-Aleutian subduction
      zone. In *AGU Fall Meeting Abstracts* (Vol. 1, p. 1565).
Bender, A. M., Witter, R. C., Rogers, M., & Saenger, C. P. (2013, December). Stable isotope values in
      coastal sediment estimate subsidence near Girdwood during the 1964 great Alaska earthquake. In *AGU Fall*
      Meeting Abstracts (Vol. 1, p. 1623).
Witter, R. C., Carver, G. A., **Bender, A. M.**, Briggs, R. W., Gelfenbaum, G. R., & Koehler, R. D. (2013,
      December). Six large tsunamis in the past ~1700 years at Stardust Bay, Sedanka Island, Alaska. In *AGU*
      Fall Meeting Abstracts (Vol. 1, p. 08).
Bender, A. M., Amos, C. B., Bierman, P. R., Rood, D. H., Sorsby, S. J., Kelsey, H. M., & Ladinsky, T. C.
      (2014, December). Differential Uplift and Incision of the Yakima River Terraces. In *AGU Fall Meeting*
      Abstracts (Vol. 1, p. 4669).

Professional Organization Memberships:
- American Geophysical Union (2012-present)
- Geological Society of America (2013-present)